

---

**University of Alberta**

**Development of Photonic Crystal  
Display Devices**

by

**Joshua Dirk Krabbe**

A thesis submitted to the Faculty of Graduate Studies and Research  
in partial fulfillment of the requirements for the degree of

**Master of Science**

in

**Micro-Electro-Mechanical Systems (MEMS) and Nanosystems**

**Electrical and Computer Engineering**

©Joshua Dirk Krabbe

Spring 2011

Edmonton, Alberta

Permission is hereby granted to the University of Alberta Libraries to reproduce single copies of this thesis and to lend or sell such copies for private, scholarly or scientific research purposes only. Where the thesis is converted to, or otherwise made available in digital form, the University of Alberta will advise potential users of the thesis of these terms.

The author reserves all other publication and other rights in association with the copyright in the thesis and, except as herein before provided, neither the thesis nor any substantial portion thereof may be printed or otherwise reproduced in any material form whatsoever without the author's prior written permission.

---

to Dr. Eva Nosal who got me started down this road

---

## **Abstract**

This thesis investigates technologies directed towards developing photonic crystal display devices. A switching technology based on dye electrophoretic motion within a 1D porous photonic crystal was developed. Dissociated absorbing dye species were moved through the assembled device and reflectance was controllably altered by up to 0.4. Refinement of fabrication techniques yielded a slow switching device, whose time-resolved reflectance data was analyzed. A wavelength dependence of the device switching speed was observed. This phenomenon was described by modelling where bandgap effects match observation.

These devices may be improved by employing a 3D photonic crystal. We developed a nanoimprint lithography technique for seeding films deposited by GLAD for the fabrication of 3D square spiral photonic crystals. Parameters for patterning a precisely defined mould pattern using electron beam lithography were established. A large area diamond:1 square spiral photonic crystal was fabricated on the nanoimprinted seeds, and it exhibited a visible wavelength bandgap.

---

## Acknowledgements

I am grateful to both those people who have made me a better researcher as well as those who have made me a better person over the course of the years of this degree. Those that both pushed and pulled on this project in various ways always with the intent to make it better: the members of the Glancing Angle Deposition research group, especially Dr. Michael Brett for creating an environment so conducive to doing state-of-the-art research and Dr. Michael Taschuk for much guidance and direction along the way, the staff of the University of Alberta Nanofabrication facility, colleagues at the NRC - National Institute for Nanotechnology, and others at the University of Alberta. All have all played important roles in my education.

Those that have shaped me as a person during the last years are less obvious, but inarguably more important. Some know of their contribution and others never will. Gordo Byrn, for encouraging me to live a life of conscious decision making; to invest where it is important to invest, to choose to be prepared, and to seek my highest performances. Lesley Baldwin, for having no reservations about expressing gratitude and enjoyment, and in a way teaching me to do likewise. Father Glen McDonald, for teaching me that peace is earned. Dave Roberts, for keeping an eye on me when I needed to have an eye kept on me. For showing rather than saying what are the most important things in both life and friendship. Molly Wizenberg, for often

---

reminding me to savour instead of to consume. The Rising Stars, for cultivating an environment where it is easy to stretch yourself and reach new heights. Frank Conroy for painting a picture of the need to re-imagine talent and skill in new stages of life. Rick VanManen, for teaching me to listen. Alan Couzens for often naming the difference between the best way and the easy way. Aaron Pleitner, for great discussions about what is possible but not worthwhile, and exploring and sharing alongside me how far is too far. Dad, for showing grace and hope in the face of pain and frustration. For being an example that love even at its best isn't outside the scope of plain old reality.

Finally I am grateful to the sources of funding that made this research possible, the Natural Sciences and Engineering Research Council of Canada, Alberta Innovates Technology Futures, the Informatics Circle of Research Excellence, and Micralyne Inc.

# TABLE OF CONTENTS

|   |          |
|---|----------|
| Abstract . . . . .                                  | iii      |
| Acknowledgements . . . . .                          | iv       |
| Table of Contents . . . . .                         | vi       |
| List of Figures . . . . .                           | x        |
| List of Notation . . . . .                          | xiii     |
| <b>1 Introduction</b>                               | <b>1</b> |
| 1.1 Preamble . . . . .                              | 1        |
| 1.2 Introduction . . . . .                          | 2        |
| 1.3 Concept Motivation . . . . .                    | 3        |
| 1.4 Concept . . . . .                               | 6        |
| <b>2 Scientific Background</b>                      | <b>8</b> |
| 2.1 Background . . . . .                            | 8        |
| 2.1.1 Photonic crystals . . . . .                   | 9        |
| 2.1.2 One dimensional photonic crystals . . . . .   | 10       |
| 2.1.3 Three dimensional photonic crystals . . . . . | 11       |

TABLE OF CONTENTS

---

|          |  |           |
|----------|--|-----------|
| 2.2      | Glancing angle deposition . . . . .                | 14        |
| 2.2.1    | 1D photonic crystals produced by GLAD . . . . .    | 19        |
| 2.2.2    | 3D photonic crystals produced by GLAD . . . . .    | 21        |
| 2.3      | Laser dye . . . . .                                | 22        |
| 2.3.1    | Laser dye in periodic media . . . . .              | 23        |
| 2.4      | Optical switching with electrophoresis . . . . .   | 26        |
| 2.5      | Nanoimprint lithography . . . . .                  | 28        |
| <b>3</b> | <b>An Electrophoretic Cell</b>                     | <b>31</b> |
| 3.1      | Introduction . . . . .                             | 31        |
| 3.2      | Design considerations . . . . .                    | 32        |
| 3.3      | Measurement apparatus . . . . .                    | 35        |
| 3.4      | First generation device performance . . . . .      | 39        |
| 3.4.1    | Enhancements to first generation devices . . . . . | 44        |
| 3.5      | Second generation device performance . . . . .     | 45        |
| 3.5.1    | Improved optical control . . . . .                 | 50        |
| 3.6      | Summary . . . . .                                  | 53        |
| <b>4</b> | <b>Time Response of the Switching Cell</b>         | <b>54</b> |
| 4.1      | Introduction . . . . .                             | 54        |
| 4.2      | Response times . . . . .                           | 55        |
| 4.2.1    | Quantifying the time response . . . . .            | 57        |

TABLE OF CONTENTS

---

|          |   |            |
|----------|---|------------|
| 4.2.2    | Modelling the wavelength dependence of optical re-<br>response times . . . . .          | 62         |
| 4.3      | Summary . . . . .   | 71         |
| <b>5</b> | <b>3D Photonic Crystals</b>   | <b>72</b>  |
| 5.1      | Introduction . . . . .  | 72         |
| 5.1.1    | Effect of seeding on film morphology . . . . .  | 75         |
| 5.1.2    | Fabrication of seeded substrates for GLAD . . . . .                                     | 78         |
| 5.2      | Electron beam lithography fabrication of a nanoimprint lithog-<br>raphy stamp . . . . . | 80         |
| 5.2.1    | Positive resist electron beam lithography . . . . .                                     | 80         |
| 5.2.2    | Determining an appropriate exposure dose . . . . .                                      | 83         |
| 5.2.3    | Quartz stamp processing . . . . .   | 91         |
| 5.3      | Imprint lithography of seeds . . . . .  | 93         |
| 5.4      | Deposition of square spiral photonic crystals by GLAD . . . . .                         | 95         |
| 5.4.1    | Optical characterization . . . . .  | 97         |
| 5.5      | Summary . . . . .   | 98         |
| <b>6</b> | <b>Conclusions and Directions for Future Work</b>                                       | <b>101</b> |
| 6.1      | Research summary . . . . .  | 101        |
| 6.2      | Short term future research suggestions . . . . .  | 103        |
| 6.3      | Avenues for future long term research . . . . .   | 105        |

TABLE OF CONTENTS

---

**References**

**107**

## LIST OF FIGURES

|     |   |    |
|-----|---|----|
| 2.1 | GLAD apparatus . . . . .  | 16 |
| 2.2 | Three basic GLAD nanostructures . . . . .   | 17 |
| 2.3 | Three basic GLAD nanostructures . . . . .   | 18 |
| 2.4 | Scanning electron microscope image of a TiO <sub>2</sub> Bragg stack . . . . .              | 20 |
| 2.5 | Optimized geometry of a square spiral photonic crystal post . . . . .                       | 22 |
| 2.6 | Methylene blue absorption and fluorescence spectra . . . . .                                | 24 |
| 2.7 | Example geometry affording electrophoretic switching of a high reflectance system . . . . . | 27 |
| 3.1 | Structure of the assembled switching cell . . . . .   | 36 |
| 3.2 | Reflectance measurement apparatus . . . . .   | 37 |
| 3.3 | Reflectance states in addressed and unaddressed 8 and 16 period Bragg stacks . . . . .      | 42 |
| 3.4 | Signal drift over a period of 80 seconds . . . . .  | 43 |
| 3.5 | Contributing spectra to functioning of second generation devices . . . . .                  | 47 |

LIST OF FIGURES

---

|     |  |    |
|-----|--|----|
| 3.6 | Addressed states of second generation devices at three voltages.   | 49 |
| 3.7 | Dye cell addressing polarity and corresponding dye motion .  | 51 |
| 3.8 | Increasing switch range amplitude with voltage . . . . .   | 52 |
| 4.1 | Time series of second generation cell switching . . . . .  | 56 |
| 4.2 | Exponential fits to time series data . . . . .   | 58 |
| 4.3 | Time constants of exponential decay response observed in de-<br>vice operation . . . . .                               | 60 |
| 4.4 | Comparison of optical constants required to model a uniform<br>absorber and methylene blue . . . . .                   | 65 |
| 4.5 | Demonstration of relative absorption strength exhibited by<br>uniform absorber in photonic crystal structure . . . . . | 68 |
| 4.6 | Simulated spectrum of photonic crystal infiltrated with methy-<br>lene blue dye . . . . .                              | 70 |
| 5.1 | GLAD growth on seeded and unseeded substrate for compar-<br>ison . . . . .   | 77 |
| 5.2 | Stamp formation and thermal imprinting process . . . . .   | 81 |
| 5.3 | Patterned holes in PMMA resist . . . . .   | 86 |
| 5.4 | Sequence of images characteristic of steps in the hole width<br>measurement algorithm . . . . .                        | 87 |
| 5.5 | Results of preliminary investigation of lattice-dose relation-<br>ship to hole size . . . . .                          | 88 |

LIST OF FIGURES

---

|     |   |    |
|-----|---|----|
| 5.6 | Secondary investigation of lattice-dose combination yielding<br>a 25% hole width recipe . . . . . | 90 |
| 5.7 | Scanning electron micrographs of seeds fabricated by nanoim-<br>print lithography . . . . .       | 94 |
| 5.8 | Scanning electron micrographs of TiO <sub>2</sub> photonic crystal . . . . .                      | 96 |
| 5.9 | Normal incidence reflectance spectra of square spiral pho-<br>tonic crystal . . . . .             | 99 |

## LIST OF NOTATION

|                       |   |
|-----------------------|---|
| $\langle 100 \rangle$ | ..... Si crystal orientation that may be cleaved into squares |
| 1D                    | ..... One Dimensional   |
| 2D                    | ..... Two Dimensional   |
| 3D                    | ..... Three Dimensional                                       |
| $\alpha$              | ..... Angle of vapour incidence (Degrees)                     |
| $\sim$                | ..... Approximately   |
| $c$                   | ..... Square spiral vertical pitch                            |
| $C_1$                 | ..... Surface fit parameter (Unitless)                        |
| $C_2$                 | ..... Surface fit parameter (Nanometers)                      |
| $C_3$                 | ..... Surface fit parameter (Nanometers)                      |
| $C_4$                 | ..... Surface fit parameter (Unitless)                        |
| $CF_4$                | ..... Tetrafluoromethane                                      |
| $CHF_3$               | ..... Trifluoromethane  |
| $Cl^-$                | ..... Chloride anion  |
| DC                    | ..... Direct current  |

## LIST OF NOTATION

---

|                                |       |   |
|--------------------------------|-------|---|
| FCC                            | ..... | Face center cubic                                   |
| GLAD                           | ..... | Glancing angle deposition                           |
| hcp                            | ..... | Hexagonally closest packed                          |
| H <sup>+</sup>                 | ..... | Hydrogen cation                                     |
| H <sub>2</sub> O <sub>2</sub>  | ..... | Hydrogen Peroxide                                   |
| H <sub>2</sub> SO <sub>4</sub> | ..... | Sulphuric acid                                      |
| IPA                            | ..... | Isopropyl Alcohol                                   |
| ITO                            | ..... | Indium Tin Oxide                                    |
| $I_{\infty}$                   | ..... | Reflectance final value (/1)                        |
| $I_o$                          | ..... | Reflectance initial value offset (/1)               |
| $I(t)$                         | ..... | Reflectance time series data (/1)                   |
| $\lambda$                      | ..... | Wavelength (Meters)                                 |
| L                              | ..... | Square spiral horizontal arm length                 |
| MF-CD26                        | ..... | Commerical metal ion free developer from Microposit |
| MIBK                           | ..... | Methyl isobutyl ketone                              |
| n                              | ..... | Index of refraction                                 |
| NXR-1025                       | ..... | Commerical thermal imprinting resist from Nanonex   |
| O <sub>2</sub>                 | ..... | Oxygen  |
| OH <sup>-</sup>                | ..... | Hydroxide anion                                     |
| $\phi$                         | ..... | Substrate rotation angle (Degrees)                  |
| PMMA                           | ..... | Polymethyl Methacrylate                             |
| PVD                            | ..... | Physical vapour deposition                          |

## LIST OF NOTATION

---

|                      |       |   |
|----------------------|-------|---|
| $r$                  | ..... | Square spiral arm cross section radius            |
| sccm                 | ..... | Standard (1 atm 20°C) cubic centimeter per minute |
| $\sigma$             | ..... | Standard deviation                                |
| SEM                  | ..... | Scanning electron microscope                      |
| SiO <sub>2</sub>     | ..... | Silicon dioxide                                   |
| $\tau$               | ..... | Time constant of optical response (Seconds)       |
| $t$                  | ..... | Time (Seconds)                                    |
| $t_{turning\ point}$ | ..... | Time of onset of electrical switch (Seconds)      |
| TiO <sub>2</sub>     | ..... | Titanium dioxide                                  |
| UV                   | ..... | Ultra violet light                                |
| $V_{DC}$             | ..... | Direct current bias voltage (Volts)               |
| $V_{pp}$             | ..... | Peak to peak voltage (Volts)                      |

# CHAPTER 1

## INTRODUCTION

### 1.1 Preamble

It was at the time of the first semiconductor lasers and when optical fibers were first used as communication lines that the characteristics of the field of photonics were defined. Studying the creation, control and behaviour of light was a distinct development beyond thinking about how light could be simply described. Whether light is a particle or a wave is not such an important question in the field of photonics. The applicable questions are rather phrased with a different mindset: How can light's wave-like or particle-like natures be exploited to a technological end?

It is thinking about light in this manner, using a viewpoint intent on both studying and exploiting physical phenomenon that has led scientists and engineers to make huge progress in research in recent years and decades. Pho-

tonics research benefits from tackling difficult theoretical questions because they often later offer the keys to utilizing the associated physics as part of a consumer application. Over the past decades a whole host of tools have been developed by photonics researchers. These tools are the answers to many of the difficult theoretical problems that have been studied and solved in years past. It is through creative thinking, and sometimes exploratory research, that the knowledge of the photonics field may be engineered into the applications that drive the lucrative industry. The work in this thesis is a body of fabrication, calculation, simulation, and endless experimentation, but it is also a creative combination of informed speculation exploiting previous work's theoretical findings. The physical phenomenon described herein were not discovered in a eureka moment but rather arose as the result of asking the question: How can the nature of light's interactions with matter be exploited to a technological end?

## **1.2 Introduction**

Photonics, by a more practical definition, is concerned with the formation, transmission and detection of photons. Applications within the field are developed by building upon these three pillars. In many applications it is the specifics regarding photon transmission that form the distinguishing features, especially in the information processing industry. Long term

visions in photonics include all-optical computing through circuitry developed based on photon flow. This might surpass the state of the art in information processing done today, where computation is based on controlling electron flow. Such systems have not yet been fully realized, but hybrid optical-electronic devices that outperform their all-electrical counterparts continue to bait imaginations and lead researchers in this direction.

The photonic crystal is an optical material that enables development of many technologies in photonics. A photonic crystal is neither a crystal nor a material in the most common uses of those words. If a normal material or crystal's properties are characterized by its **composition**; a photonic crystal's properties are defined by its **architecture**. The photonic crystal's constitution, how it is arranged and structured, is the feature that gives it interesting properties that may be exploited and used.

### 1.3 Concept Motivation

Design of tunable photonic crystals has employed many methods. The photonic crystal's optical spectrum is based in most basic terms on the arrangement of the material in the micro or nano structure and on the constituent substances' optical properties. The tuning must be therefore be based on either modifying the lattice parameter that describes the periodicity of one or of many of the materials' refractive indices. Making such adjustments has

the power to control the characteristics exhibited in the photonic crystal's spectral properties. Modifying lattice parameters will have a color shifting effect on the optical bandgap wavelengths. Adjusting refractive index typically largely changes the optical bandgap strength or intensity and has smaller effects on wavelength.

Perhaps the simplest and most intuitive method for photonic crystal tuning is to create a photonic crystal that may be stretched or compressed. Mechanically deforming a properly constructed nanostructure would directly influence the lattice parameters, and indirectly influence the refractive indices of the materials as they were subject to strain. This method suffers from difficulty in applying precise amounts of strain uniformly to a highly ordered structure. Nevertheless, the performance of such devices has been quite successful [1]. Generally though, strains introduced through mechanical stress result in changes in one dimension only, irrespective to the number of dimensions of periodicity in the crystal. Swelling a crystal lattice by chemical means generally overcomes this obstacle [2]. Introducing changes to the lattice parameters in all three dimensions is possible, however, it is generally not reversible on reasonably short time scales.

Other methods similarly exhibit unreasonably slow switching speeds and are no more applicable for display functionality than the aforementioned chemically controlled photonic crystal devices. Infiltrating a solid but porous photonic crystal with mixed liquids of highly controlled refractive

index may accurately tune an optical stop band but the timescale of such infiltrations is slow and subject to long periods of settling [3]. The same applies to methods employing capillary action to migrate some liquid into a photonic crystal [4] and generally every method employing a thermally induced phase transition [5–8].

Control based on a magnetic field or electric field generally addresses the issue of slow speeds. Magnetically induced particle motion may alter a crystal's lattice parameter in one dimension and this has been used to great effect in creating layered colloidal ferromagnetic particles with fast responses and highly accurate control [9]. Electrical control has generally been used in concert with liquid crystals infiltrating a photonic crystal [6, 10, 11]. The alignment of liquid crystals by electrical field can result in a controlled birefringence within a photonic crystal, and while such an effect exhibits behaviour in three dimensions, the directionality of any one response is strictly singular.

The method described herein utilizes an electric field to tune the optical bandgap but also relies on species migration over short distances, several lattice parameters in length. This method should be categorized amongst the quick responding photonic crystal tuning technologies, as it has potential to switch quickly. Subsequent optimizations could improve this technique whereas a thermal change or complete infiltration simply does not have the potential to categorically become a quickly responding system.

Our method exhibits an effect that is three dimensional by its nature. This is unique among other tuning techniques controlled by magnetic or electric fields. The dye ions' presence or absence within the photonic crystal is controlled by electric fields, and their motion is restricted to a single axis of migration within the device; however, the dye's optical properties are displayed in all three dimensions. (The optical properties are a synthesis of an omnidirectional absorber, and that of the photonic crystal). This technique may be applied to a photonic crystal with any dimensionality. Material limitations, as will be shown in Chapter 5 will prevent employing this technique to modulate a complete photonic bandgap in three dimensions. However, dye effects in concert with a three dimensional pseudobandgap are not handicapped by one dimensional obstacles such as liquid crystal or magnetic field orientation.

## **1.4 Concept**

This thesis' motivation is to develop a reflector with controllable spectral properties based on photonic crystals fabricated by glancing angle deposition (GLAD). Tunable photonic crystal technologies have been previously established based on a wide variety of methods but the technique used herein is a unique union of two different categories of optical behaviour. The combination of strongly absorbing dye ions with a photonic crystal op-

tical bandgap permits an interaction of optical effects. By controlling this interaction within a device it is possible to create a unique set of spectral properties and controllably tune the system's behaviour.

This work combines photonic crystals with the controlled electrophoretic motion of an absorbing laser dye. Chapters 3 & 4 focus on the development and characterization of a one dimensional photonic crystal device. A titanium dioxide Bragg stack photonic crystal is deposited by GLAD on a transparent conducting electrode and the reflectance spectrum is monitored as a solution of methylene blue dye is infiltrated into the pores of the film. Applying an electric voltage across the cell controls the motion of the dye molecules and these characteristics are described thoroughly in Chapter 4. Chapter 5 expands the work beyond one dimensional photonic crystals to three dimensions using seeded substrates and growth of square spiral films. The work's focus is on fabricating the stamp for the nanoimprint lithography process as seeding is the most critical step in 3D photonic crystal growth. Basic optical properties of the square spiral films deposited on these seeds are presented.

## CHAPTER 2

### SCIENTIFIC BACKGROUND

#### 2.1 Background

This thesis is based on studying the interplay between two sets of optical properties; a coloured laser dye's absorptive properties, and a photonic crystal's optical bandgap. By controlling the position of the dye molecules using an electric field, a previously unpublished method to manipulate an optical reflectance spectrum has been developed. This body of research is new but it is heavily built on work that has previously been done. Like much of the progress in the photonics field it has required thinking in a new way about phenomena that have been observed but not exploited. The basis for this thesis is rooted in a diverse collection of optical phenomena and electrical engineering microfabrication techniques; a brief survey is presented here.

### 2.1.1 Photonic crystals

A photonic crystal is most fundamentally a periodically ordered arrangement with large spatially varying dielectric constant [12], which results in a situation where light of wavelengths comparable to that of the structure's periodicity interacts strongly with the medium. Photon energies corresponding to these wavelengths may be understood to be forbidden in a similar way to how electronic energies are forbidden in a semiconductor bandgap. Similar terminology is used to describe the phenomena that arise, as a photonic crystal is said to possess a photonic bandgap or optical bandgap.

When full-spectrum light is shone onto the surface of a photonic crystal these forbidden-energy photons will be reflected while wavelengths not matching that of the photonic bandgap are transmitted. This bandgap may exist for photon transmission in the same number and orientation of directions as the periodicity that exists in the photonic crystal. A 1D photonic crystal will exhibit a characteristic reflection spectrum in one dimension along the axis of periodicity which will distort under off-axis examination. A 2D photonic crystal will display these characteristics within a plane, and a 3D photonic crystal will exhibit characteristic spectra when examined from any angle.

### 2.1.2 One dimensional photonic crystals

A one dimensional photonic crystal may be viewed as many reflecting surfaces in a distinctly patterned construct. Light interference has been well understood since the pre-photonics days when light was first described as a wave. It is no wonder, therefore, that long before scientists and engineers began to speak of photonic crystals using bandgap vocabulary the phenomenon was well understood. Some of the earliest work on the topic was done by William Bragg and Felix Bloch, after whom the concepts of Bragg stacks and Bloch waves are named. Wave propagation in a 1D stratified medium was well understood by the time Born and Wolf published their foundational book on the topic of optics in 1959 [13]. Since then, models aided greatly by strong computing power have facilitated descriptions of the phenomenon that are far more intricate and precise. However, at the design level, the early and general results regarding dielectric periodic media already yielded the ability to calculate and predict a material structure's spectral response. This knowledge led to the thin film engineering capability of fabricating materials with controlled and tuned reflection and transmission properties.

The simple multilayered film with a one dimensional periodic structure presents a bandgap which is characterized by suppressed transmission perpendicular to the layers' plane. The width of the bandgap is increased by

increasing the refractive index contrast of the constituent layers. The optical bandgap's center wavelength matches the optical path length through one period of the photonic crystal's structure. Complete bandgaps in one dimension may be created [14] but the wavelengths to which bandgap properties are shown apply to only narrow cone of light whose optical path length corresponds to the optical path lengths for prohibited photonic states. Consequentially, a one dimensional photonic crystal's properties are established precisely and accurately for that dimension only.

### **2.1.3 Three dimensional photonic crystals**

The three dimensional photonic crystal was proposed by Yablonovitch in 1987 [15]. His motivation was to prevent the passage of photons at a specific frequency. Yablonovitch hoped to improve efficiency of lasers, transistors and solar cells through their use, an early indication that the concept would present many more possibilities. Later the same year, John [16] proposed that the disorders in a periodic structure would permit localization of photons within the material, a necessary building block for using photonic crystals for transmission purposes as a waveguide. Fabricating a three dimensional photonic crystal would prove to be a challenge for the scientific community. The structures must be fabricated with a high degree of precision in all three dimensions to result in an optical material whose periodic properties would create a complete bandgap. A 3D photonic crystal exhibits

bandgap properties akin to the one dimensional case, where the bandgap center wavelength is equal to the optical path length through one period of the structure, but this occurs at the same wavelength when characterized in any orientation. This necessitates periodicity in all three dimensions on a very nearly identical scale. The bandgap width (typically measured as a percentage of the bandgap center wavelength) is the intersection of the bandgaps over all orientations through a crystal, or equivalently all orientations through a unit cell of the crystal. If some such wavelength exists, the 3D bandgap is said to be complete. If the photonic bandgap wavelength domains that exist for all directions do not all simultaneously overlap at some wavelength then a complete bandgap does not exist, and the material is said to exhibit a pseudobandgap.

The most obvious means by which a three dimensional uniform periodicity may be created is through the close-packing of spheres. The localization effect encountered by photons interacting with such a medium hinted that such a structure nearly possessed a bandgap [17]. The theoretical calculation done by Ho *et al.* in 1990 [18] reignited the optimism existing at the time [15,16,19,20] that very simple three dimensional lattices fabricated directly by self-assembly would exhibit complete bandgap photonic crystal properties. Ho's assertion that the closest packing structures failed to exhibit a complete bandgap wasn't broadly correct, as some FCC lattice structures have since been calculated to be candidates for complete bandgap

photonic crystal formation [21]. These structures however, are not immediately amenable to fabrication based solely on self-assembly [22] (and references therein) and require a measure of control in addition to self-assembly. However, Ho *et al.* proposed another periodic structure in three dimensions which should display a complete photonic bandgap. A diamond lattice structure was deemed capable of producing a bandgap if housing spheres or voids [18] and later other lattice structures based on this structure [23] would be shown to do the same. The methods by which a diamond-like periodic structure may be constructed is limited once the scale of fabrication is reduced below millimetre (microwave) wavelengths [24]. Telecommunication wavelengths around 1.5 microns present significant challenges in fabricating this complicated structure. Optical wavelengths, at around a third the scale, posed even greater challenges.

A variety of microstructures exhibiting periodic arrangements that may yield a complete bandgap have been discovered. The first complete bandgap photonic crystal structure fabricated, referred to as yablanovite, was composed of three arrays of holes drilled into a semiconductor at precise angles [25] yielding a slightly distorted FCC lattice structure. Another technique requiring layered strips of material was subsequently developed [26] and is commonly referred to as the woodpile structure. This technique has been widely used in conjunction with direct-write techniques to fabricate complete bandgap photonic crystals in a wide range of materials [27–30].

One other method is based on precisely backfilling a colloiddally assembled opal [31]. The resulting photonic crystal may be tuned if precisely template to exhibit a complete photonic bandgap and may be fabricated on a full-wafer scale [32–34]. Further, a theoretical model that could enable switching on and off of a complete bandgap has been theoretically proposed based on this architecture but it has yet to be fabricated [35]. The square spiral microstructure was proposed in 2001 [36] and is unique amongst these other methods in that its structure is based on a diamond lattice rather than an FCC unit cell. This is the crystal structure that will be investigated in this thesis. Direct write methods to fabricate a very precise version of the diamond lattice itself have even more recently arisen [37,38]. These direct write methods, while extremely limited in production capability, have the advantage of fabricating crystal structures theoretically superior to those realized to date by other methods [39].

## **2.2 Glancing angle deposition**

Glancing angle deposition (GLAD) is a physical vapour deposition process that is particularly suited to engineer nanoscale structure into thin films during deposition, as a single step process [40–42]. The technique relies on a collimated vapour flux incident onto a substrate surface. The deposited film nucleates on the substrate surface and introduces a shadowing effect

for regions of the surface downstream from the incident flux. This is enhanced in situations where the angle of incidence is large with respect to the surface normal. In situations when the incidence angle is glancing to the surface the resulting deposited film's microstructure is greatly impacted by this shadowing effect. Greater incident angles measured with respect to the normal produce less dense films when compared to situations of near-normal incidence. Isolated vertical columns may be formed on top of the sites of nucleation if the incident flux direction rotates continuously, elevated slightly above the substrate's horizon. Controlling the incident flux's apparent location is done by affixing the substrate to a movable chuck which is controlled by two computer controlled stepper motors. These two degrees of freedom may move the substrate to facilitate growing many microstructures when an appropriate motion algorithm is employed. The GLAD apparatus is displayed in Fig. 2.1, from [43], where the angles  $\alpha$  and  $\phi$  are also denoted. Together they describe every orientation of the substrate.

The morphology type fabricated using GLAD varies based on the motion control algorithm characteristics. The porosity, post density, and the resulting effective refractive index of the film rely primarily on the deposition parameter  $\alpha$ . The post orientations at various thicknesses throughout the deposited film rely primarily on the deposition parameter  $\phi$ . Fig. 2.2, from [42] and [40], shows the variation in microstructure that occurs with a variation in rotation speed of  $\phi$  through a deposition where the parameter

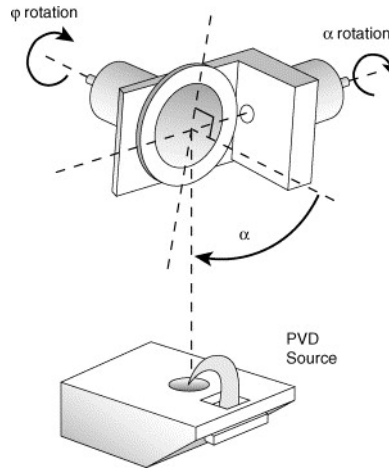


**Figure 2.1:** Illustration of GLAD deposition apparatus. Computer controlled motors drive the substrate to determine vapour flux incidence direction. A crystal thickness monitor provides feedback on the deposition rate. Reprinted from *Photonics and Nanostructures - Fundamentals and Applications*, Vol 4, Issue 1, D.A. Gish, M.A. Summers and M.J. Brett, Morphology of periodic nanostructures for photonic crystals grown by glancing angle deposition, Page 2, Copyright (2006), with permission from Elsevier.

$\alpha$  is held constant.

When a planar substrate is used the nucleation proceeds as a random process, however the initial nucleation sites may be specified through pre-patterning the substrate with bumps. The spacing of such bumps must be reasonably close to the column spacing that would naturally appear. The PhiSweep technique [44] affords an improved ability to deposit films to a less than optimally matched seed spacing. The technique decouples the post growth direction from the incident flux direction by stacking a series of smaller slanted posts on one another to create the film's overall microstructure [44]. Fig. 2.3, from [43], shows variations in film quality resulting from

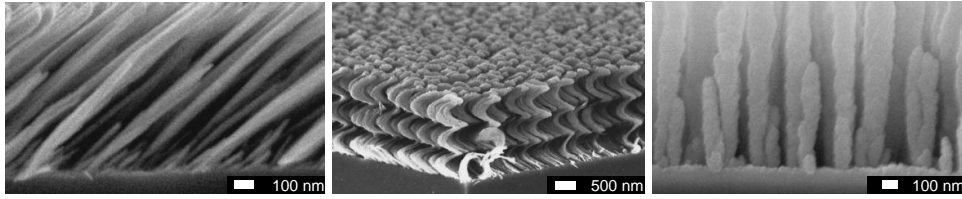


**Figure 2.2:** Three basic GLAD nanostructures fabricated with constant  $\alpha$ , the slanted post (constant  $\phi$ ), helix (gradually varying  $\phi$ ) and vertical post (rapidly increasing  $\phi$ ).

Left and right figures reprinted with permission from K. Robbie, "Advanced techniques for glancing angle deposition," *Journal of Vacuum Science & Technology B: Microelectronics and Nanometer Structures*, vol. 16, May, 1998, p. 1115. Copyright 1998, American Vacuum Society. Center figure reprinted with permission from K. Robbie, "Sculptured thin films and glancing angle deposition: Growth mechanics and applications," *Journal of Vacuum Science & Technology A: Vacuum, Surfaces, and Films*, vol. 15, May, 1997, p. 1460. Copyright 1997, American Vacuum Society.

modifications to a motion control algorithm designed for slanted posts. Using this method, control of feature spacing is possible to a degree; however multiple nucleations on a single seed, nucleations spanning multiple seeds, or nucleations between seeds may occur if the spacing control is incorrect.

GLAD has a numerous specific advantages over other techniques for creation of films with nanometre scale structures. The diversity of the PVD category lends itself to a wide versatility and therefore to an extremely wide range of potential materials. Using electron beam evaporation as the vapour flux source is typically preferred for most metals, common dielectrics and metal oxides. The use of sputtering has also been demonstrated [45]. GLAD can be used for almost any material compatible with PVD methods including pulsed-laser-deposition [46]. This versatility of multiple materials is not available with most techniques for nanoscale patterning.

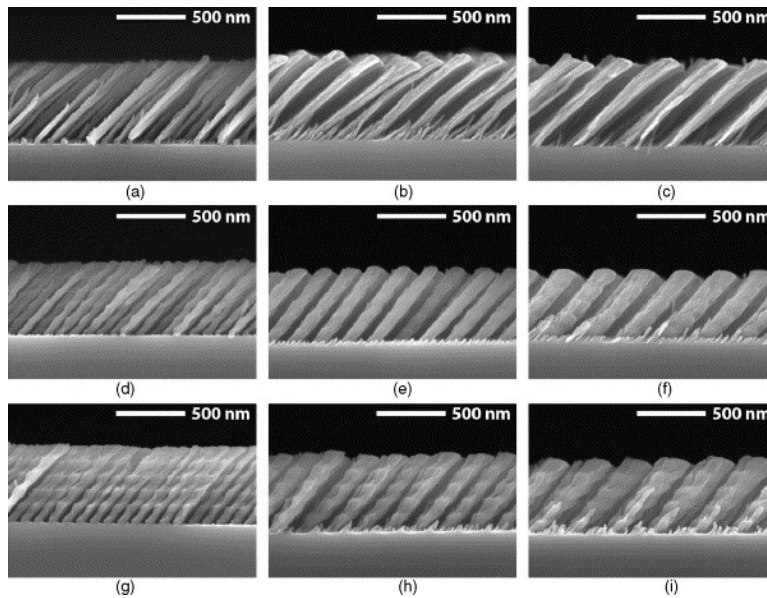


**Figure 2.3:** Side view SEM images of the Si slanted post films fabricated using (a)-(c) traditional GLAD, (d)-(f) PhiSweep with a sweep angle of  $30^\circ$  and (g)-(i) PhiSweep with a sweep angle of  $45^\circ$  on 100, 200, and 300 nm periodicity substrates, respectively

Reprinted from *Photonics and Nanostructures - Fundamentals and Applications*, Vol 4, Issue 1, D.A. Gish, M.A. Summers and M.J. Brett, Morphology of periodic nanostructures for photonic crystals grown by glancing angle deposition, Page 5, Copyright (2006), with permission from Elsevier.

The film porosity may be controlled by the growth motion algorithm and the vapour flux incidence angle. Control over film porosity makes many applications possible; the resulting high film surface area (due to the presence of many pores) may be exploited for many purposes. Various physical, chemical and biological phenomena exhibit surface area limited properties and films formed by the GLAD technique may adsorb more molecules to the surface than a planar film. This has been demonstrated by the use of GLAD films in humidity sensing applications [47].

### **2.2.1 1D photonic crystals produced by GLAD**

The one dimensional (Bragg stack) photonic crystal may be created using GLAD as follows. The porosity of a material deposited by GLAD is tied directly to its density. This enables use of the angle of incidence to precisely modify a layer of the film's effective refractive index. This is critical to forming one dimensional periodic structures such as the Bragg stack photonic crystal. The two layers' indices of refraction are controlled by altering the incident angle of the vapour flux during the deposition. High density and low density regions are generated as the substrate is continuously rotated to produce a vertical post microstructure. The layer thicknesses are chosen such that the optical path length through one period of the film is equivalent to the desired bandgap center wavelength. Fig. 2.4 shows one example of a Bragg Stack photonic crystal fabricated by GLAD. The columnar mi-

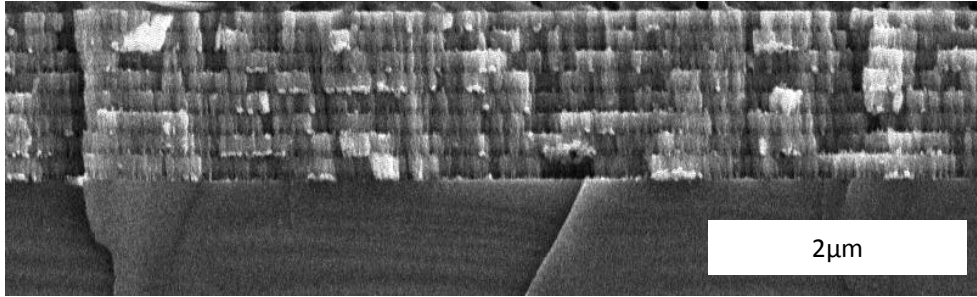


**Figure 2.4:** Scanning Electron Microscope image of an 8 period  $\text{TiO}_2$  Bragg stack Photonic Crystal. The nanostructure of the film is shown to have a porous nature.

crostructure seen in the image is indicative of a high rate of rotation of  $\phi$  where the substrate is rotated through  $360^\circ$  for each 10 nm of film growth.

The lower bound on the index of refraction is given by that of air ( $n=1$ ) and the upper bound is given by the bulk material's refractive index. Generally neither the upper nor the lower bounds are achievable and high and low index layers are composed with indices somewhere between the two. It is common practice to maximize the index contrast necessary for producing strong optical bandgap by using very high index of refraction materials when the deposition technique allows it. Titanium dioxide is a common choice of materials [47,48] in this regard and it is the material of choice for this body of work. Introduction of periodicity defects to such a system can provide more complicated and potentially useful spectral responses including narrow band-pass filters [48].

### 2.2.2 3D photonic crystals produced by GLAD

In 2001, Toader and John proposed a structure that would form a diamond-like lattice at a scale previously unachievable by any reliable means [36]. The photonic crystal developed based on their square spiral design exhibited three dimensional periodicity and yet planar uniformity (in design) across the substrate. This was in contrast to other contemporary designs which had been put forward but whose fabrication would be unachievable by any conceivable bulk manufacturing technique at small scale due to demanding a phase shift for neighbouring circular spirals [49]. The design by Toader and John was specifically amenable to fabrication by GLAD and it was successfully fabricated within months of being proposed [50,51]. Theoretically modelling the square spiral according to a parameterized architecture established a precise set of measurements to which a square spiral photonic crystal would conform. These parameters are displayed in Fig. 2.5.

The GLAD technique was soon refined by carefully modifying aspects of the motion control algorithm to successfully fabricate optimized spirals. Developing the optimal uniform structure was reduced to a challenge in control and refinement of the GLAD technique's ability to form this architecture [43,52,53]. This work continued through a number of iterations, and included techniques to prevent column broadening which significantly refined the process [54]. The square spiral photonic crystal is the forerunning can-

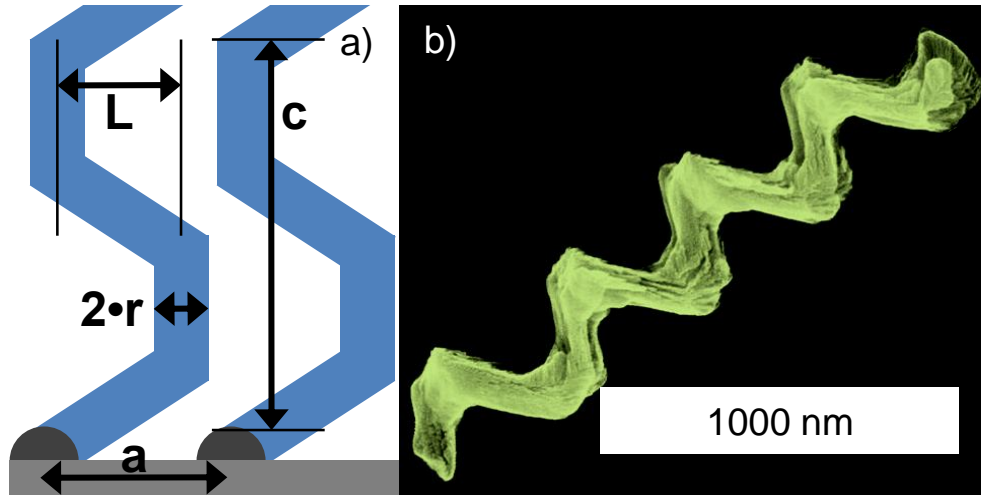


**Figure 2.5:** a) Schematic of square spiral post architecture. The dimensions conventionally used to parameterize these spirals consists of scalar values  $L$ ,  $c$ , and  $r$  in units of the lattice seed spacing  $a$ .  $L$  is the spiral width,  $c$  is the spiral pitch height, and  $r$  is the radius of the column. A right handed spiral has the second and fourth arms pointed into and out of the page respectively. b) A sample right handed spiral fabricated using  $\text{TiO}_2$ .

didate for development of applications for complete bandgap 3D photonic crystals where they are required in a large area. Its relative simplicity in processing when compared with other methods makes it a competitive process for microfabrication of 3D complete photonic bandgap structures [55].

### 2.3 Laser dye

Laser dyes are large organic molecules, typically possessing multiple carbon rings and ranging in molecular weight from hundreds of atomic units to a thousand atomic units [56]. The laser dye molecular electronic structure is such that it can absorb energy from a large spectral region. Dye lasers

applications have led to dye characterization and refinement for laser dyes operating in the optical and near infrared regions of the spectrum. The laser dye's absorption spectrum characteristically does not completely overlap its fluorescence spectrum, which is spread over a range of wavelengths at lower energies than the absorption spectrum. An example pair of spectra is shown in Fig. 2.6 from [57] for methylene blue, the laser dye used in this work.

Dye laser operation ideally occurs at a wavelength where absorption of the dye is minimal as to prevent re-absorption of the beam of stimulated emission and instead present a nearly transparent path for propagation of the light. A laser dye will only support stimulated emission when pumped into an inversion population, but the properties of strong absorption in one bandwidth and emission of the light in another bandwidth are maintained when an inversion population does not occur. This specific phenomenon, favoured for high quality laser operation, has led to selecting and developing dyes with such properties. A dye that has a very specific colour for its absorption spectrum and high absorptivity at those wavelengths works best in a dye laser. It is precisely this property that was desired for use with this research.

### **2.3.1 Laser dye in periodic media**

The inclusion of laser dyes in periodic media has been examined in recent years; the primary motivation has been the development of a laser requiring

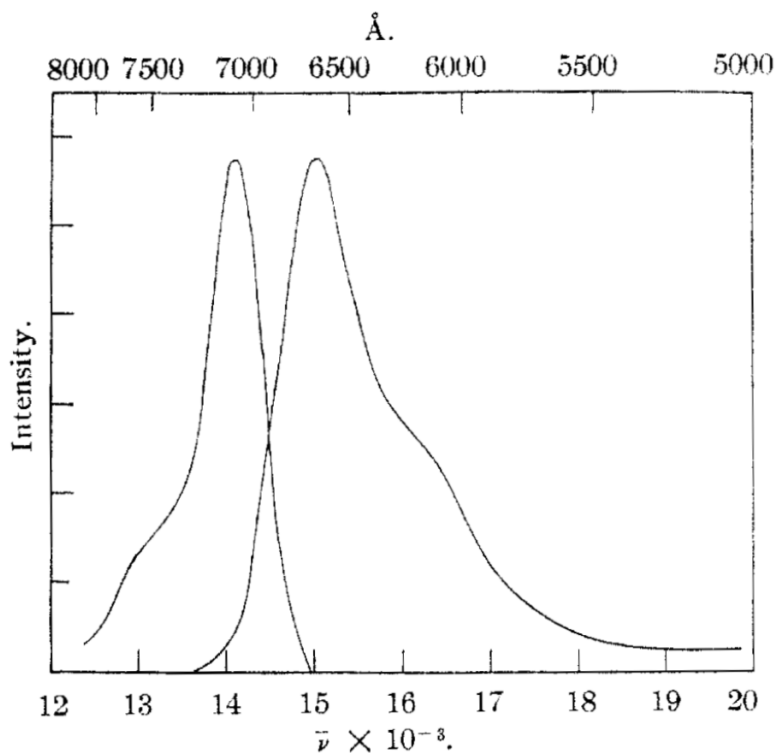


**Figure 2.6:** The absorption and fluorescence of methylene blue: right, absorption curve in glycerol at room temperature; left, emission curve in glycerol at  $-25^{\circ}$ ; the ordinates are direct microphotometer readings, no corrections having been made for plate character; nor has correction been made for self absorption, as shown by the rapid falling off on the high frequency side of the fluorescence curve.

Reprinted with permission from G. N. Lewis, O. Goldschmid, T. T. Magel, J. Bigeleisen, Dimeric and Other Forms of Methylene Blue: Absorption and Fluorescence of the Pure Monomer, *Journal of the American Chemical Society*, Vol 65, Issue 6, Page 1154, Copyright 1943 American Chemical Society.

no resonator cavity by increasing the residence time of the emitted photons. Scattering laser light within a macroporous structure was shown to decrease the Rhodamine-6G dye emission bandwidth in a laser and simultaneously increase the peak intensity of the emission spectrum [58]. The scattering process was considered akin to extending the gain medium's useful length as the scattering facilitates a longer residency within the gain medium prior to photon escape. When investigating a one dimensional photonic crystal's ability to increase the residency time before emission it has been shown that increases in the amplified spontaneous emission by a factor of 6 are achievable [59]. Work has also been done with 3D periodic structures in the form of inverse opals, with pseudobandgaps. Emissions from rare earth luminescent species have been enhanced by this method [60] as well as the emission from laser-dye-solution-infiltrated structures [61]. In all of this research, the presence of the surrounding periodic structure increases the photon residence time, leading to an enhancement of the species' emission properties, as a greater fraction of the species may participate in the optical process. This increased photon residency has an effect which is exhibited in all observable spectra of the dye. Photon residency affects emission properties, interaction with the emitted photons is increased, and also absorption characteristics, as absorption is increased. The indication is that threshold lasing powers are decreased by the presence of the structure, fortuitously indicating that the per-molecule effect is on average greater [61].

## 2.4 Optical switching with electrophoresis

Optical switching is an important transmission control building block for photonic systems. Switching can be based on introducing absorbing or scattering particles into a critical portion within an optical device to attenuate the propagation of photons. If sufficient contrast can be developed between the state with these particles present and the state with them absent, a photonic switch can be realized. Switching may be controlled by various means but electromagnetic control is obviously a desirable choice.

One method of switching a device's optical properties is to move a pigment particle through solution by electrophoretic forces. Changing particle locations may alter the optical properties if it is brought near a surface of a substance with greater refractive index which is geometrically aligned to be totally internally reflecting light [62]. The particles must be kept away from the surface by electrostatic forces while the device is meant to allow the passage of light and then be brought into close proximity with the surface to frustrate the total internal reflection that is occurring either by absorption or scattering. One such geometry affording such an interaction is shown in Fig. 2.7. The figure, from [63], shows a method of achieving high reflectance especially at normal and near-normal angles of incidence. Incident light is totally internally reflected within the high-index glass when the pigment particles are held away from its surface and light is either absorbed or scat-

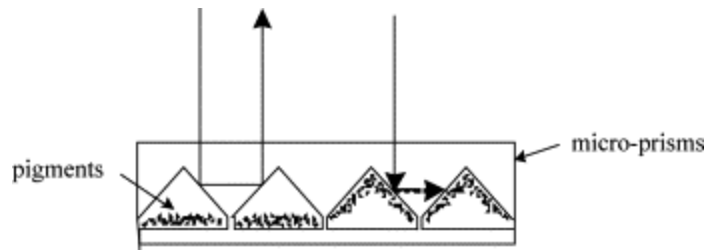


**Figure 2.7:** Schematic drawing of a high-reflectance device using micro-prisms and electrophoretic movement of pigment particles to control the reflection of light. (Not to scale) Reprinted from *Displays*, Vol 25, Issue 5, Michele A. Mossman, Vincent H. Kwong and Lorne A. Whitehead, A novel reflective image display using total internal reflection, Page 3, Copyright (2004), with permission from Elsevier.

tered when the pigments are brought in close proximity with the reflecting surface.

Fig. 2.7 is just one geometry and others have been developed. Concerns regarding the device lifetime typically arise along with a switching mechanism based on moving pigment particles. The particles in solution must all carry a charge, in the event that one loses its charge it is no longer controlled by the device's electric field and may frustrate internal reflection when undesired and not contribute to light scattering when the contribution is desired. Charged pigment particles also have the tendency to agglomerate with one another and fall into motion patterns under repeated switching which may see them migrate through the device [64]. The use of dye ions in place of charged pigment particles solves the problem of agglomeration as the molecular structure is instead an anion cation pair rather than a charged particle. The smaller size lends to more uniform distributions minimiz-

ing the effects of clustering. Frustrating total internal reflection has been demonstrated using dye molecules in the presence of surface area enhancing structures including that of a porous film deposited by GLAD [65].

## 2.5 Nanoimprint lithography

Work done on fabrication of 3D photonic crystals using the GLAD technique has historically relied upon UV photolithography, electron beam lithography, or block-copolymer patterning among other self-assembly techniques to pattern the substrates prior to deposition to create the seeding pattern [43, 50, 52, 54, 66, 67]. The limitation in scale using some techniques, the lack of reliability in pattern precision, and incredible time and financial cost, have been real barriers to fabricating seeds of high quality and quantity. The conventional techniques are described in more detail in chapter 5. Nanoimprint lithography is a method that exists to pattern seed arrays at the lattice spacing preferred for telecommunication wavelength photonic crystals or optical wavelengths, in a single step, and therefore is a quick and relatively inexpensive [68] lithography process.

Nanoimprint lithography is a method for forming a resist mask comparable to the resist mask created by an optical or electron beam lithography process. A mould is impressed to a layer of resist, a polymer, and the topographical features of the mould are copied into the resist layer. At this

point the resist is cured into the morphology of the imprinting mould; this is done by one of two methods. The first is an exposure to ultraviolet light, a mould transparent to ultraviolet light is therefore required and quartz is the material of choice for the process due to its notable rigidity and optical properties. The UV cured resist is composed of photosensitive cross linking chemicals and monomers which are to be cross linked by the activation of the photosensitive chemical once exposed [69–71]. The monomers composing the bulk of the resist must be of sufficient weight to crosslink effectively and form a compound post-exposure that will not relax back to the pre-imprinted state. The weight of the monomers however must not be so significant that they cannot flow into the recesses of the imprinting mould when subject to pressure. Thermoplastic curing is the other method possible; the resist is composed of a thermoplastic polymer and surfactant [72] with a glass transition temperature above the normal processing temperatures of deposition and etching. The resist, substrate and mould are heated above this transition temperature and the resist flows, filling the topography of the mould, before cooling. Release agents may be applied to the mould to facilitate detaching the mould from the substrate but the process is predominantly a mechanical one.

For photonic crystals the second step is optional, the pattern in the resist may be used as the seeding pattern for subsequent photonic crystal growth or it may be translated into the substrate by further etching and the pho-

tonic crystal growth proceeding from this topography. The second step in the process is analogous to the chemical developing of an optical or e-beam resist. The shape of the mould has been transferred to the surface layer of the resist layer but prior to making use of the mask the features must be vertically translated through the thickness of the resist layer to the surface of the substrate. This is done by some form of etching where resist is eliminated from compressed areas and thinned in the raised areas of the pattern. At this point a preferential etch may be employed to transfer the pattern to the substrate and then even to increase the aspect ratio.

## CHAPTER 3

# AN ELECTROPHORETIC CELL

### 3.1 Introduction

In this chapter<sup>1</sup>, experiments that confirmed a change of states in a dye infiltrated photonic crystal using an electric field are discussed. The initial goal was to achieve the largest possible reflectance change between states of the electrophoretic cell, maximizing the reflectance in one state while simultaneously minimizing it in another. The reflecting state's strength is theoretically limited by the electric field strength drawing the ions out of an optimized photonic crystal. The least reflectance is theoretically achieved by maximizing absorbing dye ion concentration in the photonic crystal when electrically addressed to accumulate dye for a non-reflecting state.

Design decisions were made to achieve these goals. Concurrently, a

---

<sup>1</sup>A version of this chapter has been published. Krabbe 2010, Proceedings of SPIE Photonics West 2010. 7609. [73]

means to characterize and analyze the device performance was iteratively developed. The co-evolution of the device with improved measurement reliability and accuracy is evident in the progression of data quality in this Chapter's figures. Not as evident are the associated skills and knowledge accumulated by having experienced those early development stages. Infiltrating devices with dye solution without bubble inclusion, the uniform spreading of glues, and decisions leading towards fabricating devices in a range of different sizes were largely based on experience, not through *a priori* calculation. Beginning the project again with a honed and refined skill set may have been faster, but doing things the wrong way before doing them the best way often proved to lend insight. For this reason, the early work is presented along with more refined data.

### **3.2 Design considerations**

GLAD was used to deposit a varying high and low index multilayer film onto transparent ITO coated glass substrates. The bandgap was aligned with the absorption spectrum of the selected dye; the fluorescence spectrum was thus slightly misaligned with respect to the photonic crystal's prohibited wavelengths. Ideally, sufficient porosity is maintained for all Bragg stack layers such that dye ions' electrophoretic movement in and out of the structure will be possible following cell fabrication.

ITO coated glass substrates were used as the transparent conducting substrates for the GLAD photonic crystal thin films. Titanium Dioxide ( $\text{TiO}_2$ ) was chosen for the GLAD film based on the criteria of high bulk index, insolubility in methanol (the solvent to be used to suspend the dye ions) and extensive past history of use with the GLAD process. Bragg stack photonic crystals were deposited in 8 and 16 layer stacks with designed total thicknesses of  $1.74 \mu\text{m}$  and  $3.07 \mu\text{m}$ , respectively. The chuck control algorithm for the GLAD process is based on a selection of the minimum angle of incidence ( $\alpha = 50^\circ$ ) of the collimated vapour flux to the surface, as pictured in Fig. 2.1. Index contrast between this relatively dense layer and more porous layers ( $\alpha = 80^\circ$ ) yields a photonic crystal with a suitable balance of continuous porosity and optical bandgap strength. The nanostructure was designed to be columnar to ensure the photonic crystal exhibited azimuthally symmetric properties. Substrate rotation was controlled to yield one rotation in  $\phi$  (see Fig. 2.1) for each 10 nm of film growth. The films were deposited at a rate of between 0.6 nm/s and 1.0 nm/s at the thickness monitor using an accelerating voltage of 6.5 kV and a current of between 300 mA and 325 mA. Deposition chamber pressure was controlled to be maintained within a  $6\text{-}9 \times 10^{-5}$  Torr range and the films were allowed to age for 7 days in atmosphere to correct sub-stoichiometric composition and allow for the optical properties to settle. The time constant describing the settling process during which optical absorption diminishes in other  $\text{TiO}_2$  films deposited by

GLAD has previously been shown to be near 30 hours. [74] Fig. 2.4 depicts the microstructure of one such film.

The design goal is to engineer a maximum contrast in reflection between the dye-infiltrated state and the plain solvent infiltrated crystal. The dye must dissociate as an anion-cation pair so as to be controllable with an electric field. Based on the choice of material for the photonic crystal ( $\text{TiO}_2$ ) the use of a dye that dissociated with  $\text{H}^+$  or  $\text{OH}^-$  ions was undesirable. The surface chemistry of the  $\text{TiO}_2$  interface is known to display photocatalytic properties and may act as a reducing agent, which may contribute additional unpredictable effects with these ions [75]. Additionally, methanol's interaction with  $\text{TiO}_2$  is known to involve these species [76] and we sought to work with other ions to stop this from playing a contributing role. Methylene blue dye (Sigma Aldrich) was selected; it has dissociation species of a chlorine anion and a heterocyclic aromatic cation, the latter which is responsible for the absorptive behaviour of the dye.

The  $\text{TiO}_2$  coated substrates were bonded using GelControl Loctite SuperGlue to a counter-electrode of another ITO coated piece of glass. A schematic diagram of the final structure is displayed in Fig. 3.1. Early devices were fabricated favouring maximizing electric field strength within the cell. The highest electric fields would result when inter-electrode separation was minimized by placing the counter electrode immediately behind the photonic crystal. The electric field strength should be a determining factor

in how great a dye concentration gradient may be established within the cell while being addressed. Thus, for first generation switching cells, errant dust particles and bits of molten TiO<sub>2</sub> landing on the surface during deposition of the TiO<sub>2</sub> photonic crystal provided the spacing between the electrodes. The inclusions' sizes that would cause the resulting inter-electrode spacing were estimated by observing the photonic crystal with a scanning electron microscope. The estimated spacing that should occur between the top of the GLAD film and the counter electrode is 3  $\mu\text{m}$ -5  $\mu\text{m}$ . Copper tape is used to make electrical contact to the ITO conducting layers and these leads are attached to the control electronics. The unobstructed operating region of the completed cells is approximately square with a side length of approximately 10 mm.

### **3.3 Measurement apparatus**

A custom optical setup was constructed to measure reflectivity, and is depicted in Fig. 3.2. A white light source passes through a beamsplitter and is incident on the cell. The light reflected from the cell passes out through the beamsplitter and is focused through a lens towards an optical fiber leading to a HR4000 Ocean Optics Spectrophotometer. An aperture was used to limit light incident to only the central portion of the working area of the switching cell entering the focusing optics. Typical aperture sizes used

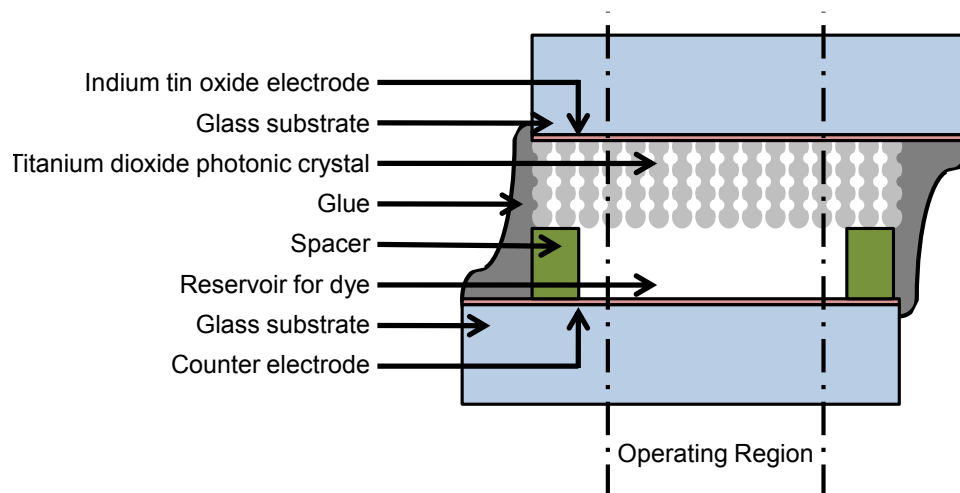


**Figure 3.1:** Schematic diagram of bonded cell. Reflectivity of the cell is measured from the top surface and dye is introduced to the reservoir from the front. The path of the incident light encounters the photonic crystal before the reservoir containing the dye. The illustration is not to scale.

ranged from 2 mm through 8 mm in diameter. Shorter integration periods are facilitated with comparable signal to noise ratios when larger apertures are used, which was especially useful for work presented in Chapter 4. An integrating interval of 30 ms is used with the OceanOptics software during data collection. The cell is oriented in the apparatus such that the substrate with the photonic crystal deposited on the surface is encountered first, followed by the small inter-electrode reservoir of methylene blue solution and finally the counter electrode. A laser is used to ensure that the surface is orthogonal to the white beam of light. Reflectance was calibrated using a silicon reference standard.

A dark recording with the spectrophotometer was taken as background

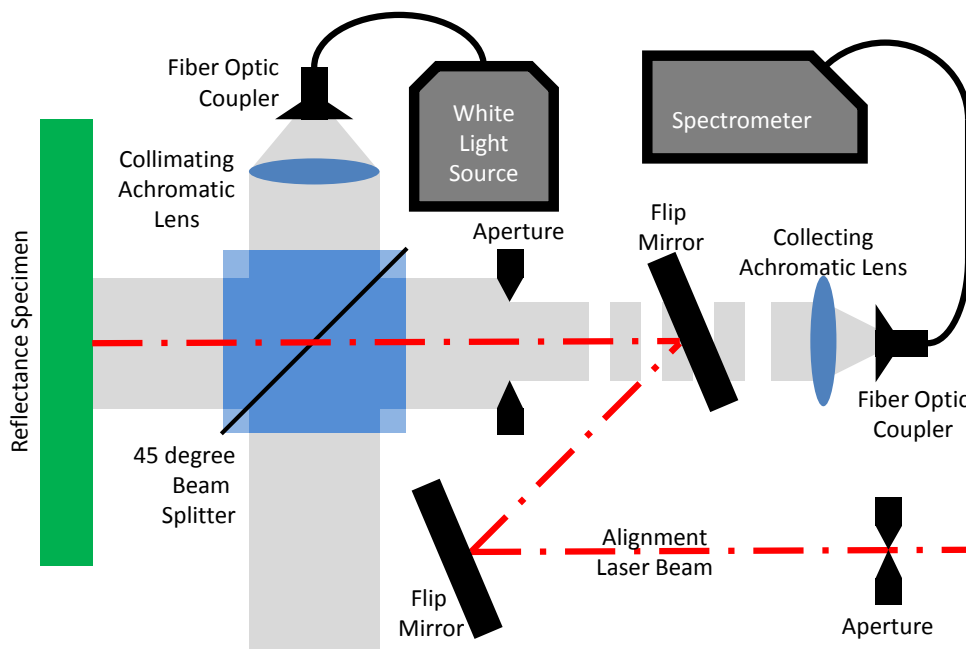


**Figure 3.2:** Reflectance measurement setup - top view. All white beam-paths are circular in cross-section.

and the silicon reference standard was measured to calibrate the intensity of the lamp before recording device data. Collecting spectral data from a sample was done after the tungsten lamp had warmed up and initial spectrum drifting had ceased, 10 minutes after the lamp had been turned on. After this warmup, intensity drift for all wavelengths following these 10 minutes of warm-up is less than 3% per hour. At wavelengths longer than 500 nm, lamp drift is even less; the output intensity is stable with constant mean and variation less than 1% ( $1\sigma$ ).

A repeatability study was performed to establish the degree of accuracy in aligning a sample within the system using the reference laser beam.

Aligning the sample using a laser reflected from the surface back down more than two meters of beam path through a 1 mm aperture was difficult for a manually aligned system. Such demands approach a kinematic mount's precision limit. Initial results were very poor, with supposedly identical results varying by more than 80% on occasion, and spectra highly distorted. This distortion error was attributed to the chromatic aberration due to a singlet lens. Coupling signal light back into the optical fibre at high focus presented massive unreliability in this system's performance.

To address repeatability, achromatic lenses with focal length 100 mm (Thorlabs AC254-100-A) were used to upgrade both lenses in the original system (Fig. 3.2). This facilitated using significantly larger apertures without including chromatic aberration at the white beam edges. By allowing an increased beam size a greater white light intensity was available and it was fed slightly unfocussed into the fiber optic coupler. Using a three dimensional translation stage and kinematic mount to align the collecting achromatic lens permitted high accuracy in coupler placement and alignment. The fiber optic coupler was centered within a  $\sim 1.25$  mm diameter beam of light. These changes to the system's optics without improving on sample orientation yielded repeatability comparable with the recording noise (shot noise  $\sim 0.7\%$  and thermal noise) of the detector when using a 100 ms integration period. Chromatic aberrations were no longer detectable as distortions in measured spectra. All reflectance measurements taken in

darkroom conditions include a 2% uncertainty between 500 nm and 800 nm wavelength when a 100 ms integration period is used. Short and long wavelengths are subject to greater uncertainty, as signal to noise ratios deteriorate rapidly below 475 nm and above 825 nm wavelength, outside the white light source's principle emitting wavelengths.

When measuring a static spectrum the integration period may be increased, or averages may be calculated over many integration periods, to greatly reduce the uncertainty in measurement. This yields measurements where alignment accounts for all of the measurement uncertainty and values are presumed to be accurate within 3% once the source's drift is accounted for. When sequential measurements are being recorded from the same sample they possess no uncertainty in sample alignment relative to one another. However, absolute uncertainty in recording each value is not reduced. When compared to one another, differences between sequential values are accurate to within 3% however the absolute uncertainty might be as high as 5%.

### **3.4 First generation device performance**

A test photonic crystal was deposited and its bandgap center wavelength measured when dipped in methanol. This enabled an experimental relationship to be determined between the TiO<sub>2</sub> photonic crystal physical periodicity and the optical path length as experienced by a photon. Direct

calculation of the desired design periodicity may be completed however they will inevitably lack a degree of specificity to the true manufacturing procedure. The typical procedure for measuring the relationship between the GLAD angle  $\alpha$  and resulting index of refraction is to deposit a series of films of varying  $\alpha$  and characterizing them by variable angle spectroscopic ellipsometry. While providing a useful starting point, these one layer depositions at a single  $\alpha$  are inadequate to precisely engineer a multilayered film's optical properties [74] because the optical path length will be impacted by each subsequent layers' precise density in the film. Additionally, the columns porous natures will be affected by deposition rate heating of the film surface. Depositing test films, characterizing them, and appropriately scaling their design parameters is a straightforward yet reliable way to align the bandgap of the photonic crystal to a specific wavelength. The test films deposited with a design periodicity of 217 nm yielded a bandgap center vacuum wavelength of approximately 745 nm when submerged in methanol. To align the bandgap center wavelength with the absorption of methylene blue at 655 the design periodicity was scaled to 191 nm. The resulting film's bandgap, it was later determined, was subsequently centered near 675 nm, suitably overlapping the absorption spectrum of the dye.

Eight and sixteen period photonic crystals were deposited by GLAD for first generation devices and cells were assembled as in Fig. 3.1. Using a syringe, a range of methylene blue in methanol solutions were applied to

the seam at the device edge. The dye mixture was allowed to wick into the device by capillary action. A square wave voltage signal is applied to the switching cell, of equal magnitude in both polarities. The duty cycle addressing the cell in both directions is set to be equal with the hope that significant amounts of dye accumulation or depletion from the photonic crystal will not occur. The driving voltage signal's period and magnitude were tuned by monitoring by an oscilloscope while voltage magnitudes are measured using the DC voltage probe as it yields superior precision in measurement. At any one wavelength, the reflectance switches from a high reflectance to low reflectance state. Sample spectra displaying the difference between such states is displayed in Fig. 3.3.

Recording reliable spectra from early devices proved challenging. During infiltration, settling times of many tens of minutes were required before the reflectance spectrum ceased to display noticeable shifts. Even when the motion of the dye by capillary action through the cell had appeared to have ceased, it was evident that dye redistribution was still occurring. Once macroscopically observable dye infiltration had ceased to progress, significant drifts in signal are clearly seen as the dye solution continued to be redistribute itself within the cell (As shown for example in Fig. 3.4). These switching cells also demonstrated a propensity to short circuit during operation and ceased to switch as an electric field could no longer be sustained between the electrodes. The short period of time that these devices could op-

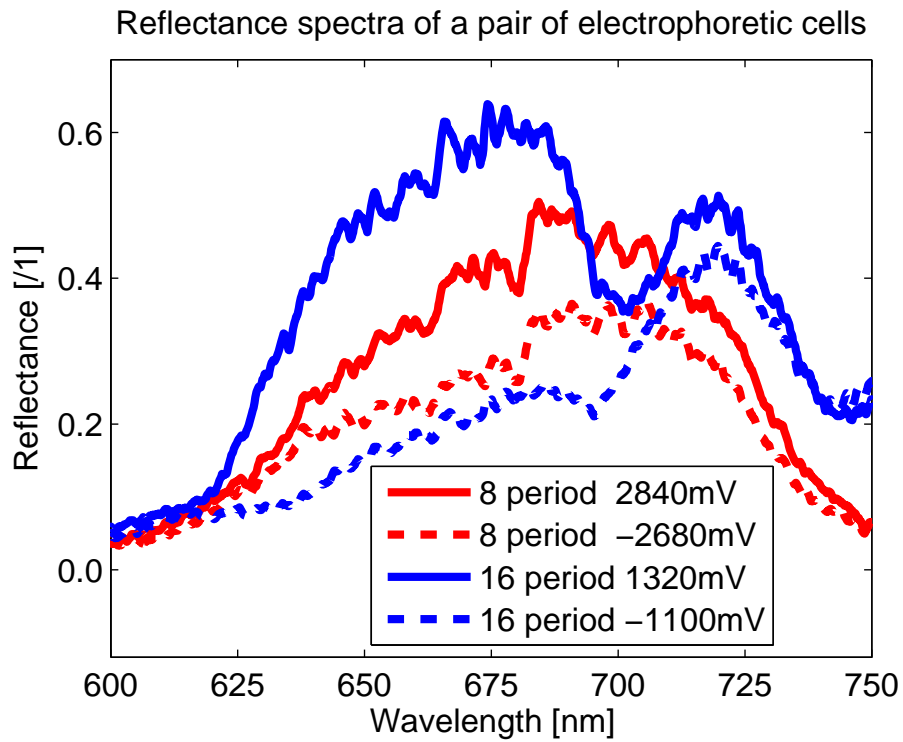


**Figure 3.3:** Reflectance spectra from 8 period (red) and 16 period (blue) Bragg stacks in both positively and negatively addressed states. Methylene blue's peak absorption occurs at 652 nm within the bandgap of the photonic crystal. Compare with Fig. 3.5 where the peak absorption is intentionally misaligned.

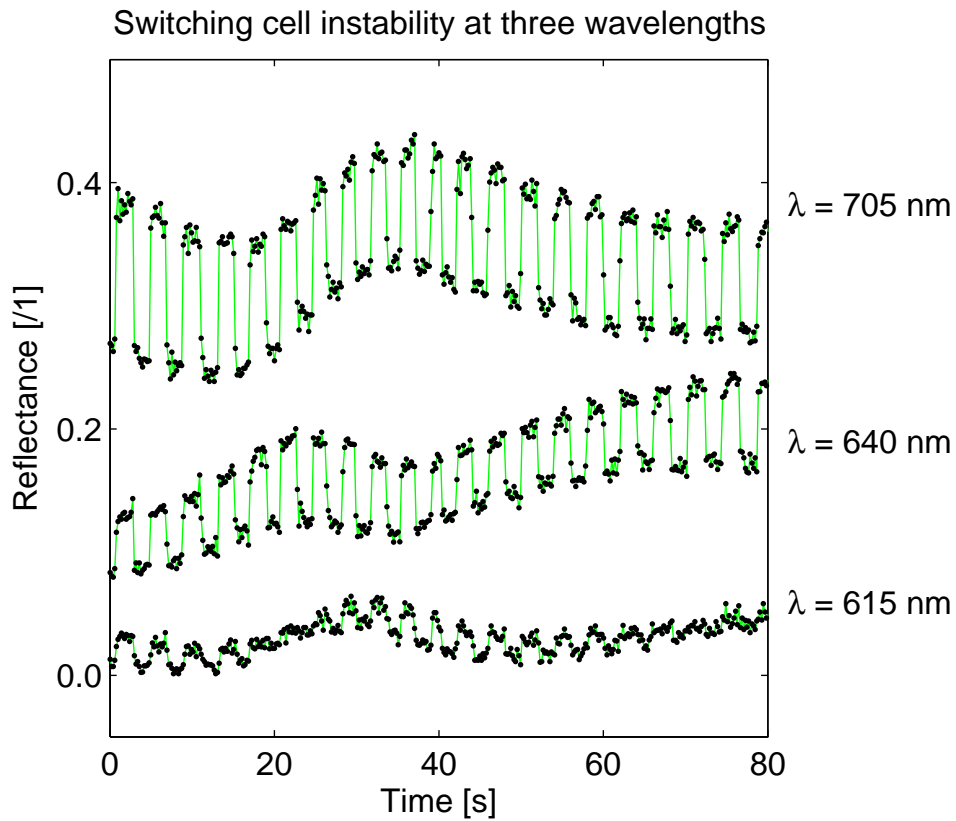


**Figure 3.4:** Evidence of signal drift due to poor dye infiltration, typical of first generation devices. Switching speeds faster than are detectable by the spectrometer are achieved due to relatively high voltages ( $2.8 V_{pp}$ ) and very small dye reservoir thicknesses.

erate before failure made it difficult to wait for them to come to equilibrium before studying the device to device repeatability. Rough observations however, indicated that the spectra under similar addressing conditions were not behaving as similarly as one might hope or expect. Some cells responded maximally to an addressing voltage in hundreds of mV while others required in excess of a thousand mV to achieve similar switching magnitudes.

### 3.4.1 Enhancements to first generation devices

Reflectance intensity drift was attributed to dye distribution and accumulation in various parts of the device. By increasing the dye reservoir size, faster infiltration could be facilitated and the increased dye reservoir volume could act as a moderating buffer against depletion effects such as all dye molecules being drawn into the cell. A larger reservoir's dye concentration varies less as the same quantity of dye is moved through the photonic crystal. This added stability was believed to help rather than hinder the device performance. Field reduction however would occur for equivalent voltages with this design modification. Nonetheless, stability in measuring results enabled the faster switching speeds observed (as in Fig. 3.4) where cells were observed to have settled nearly completely to a new addressed state within a single 100 ms spectrometer integration period.

In addition to increasing the size of the reservoir, solution strength was increased through early iterations and it soon became apparent that the best performing devices had the most dye ions accessible within them. Using a saturated methylene blue solution would maximize this benefit.

The dye's absorption spectrum spanned the entire photonic crystal optical bandgap in these devices. Drift due to dye migration across the scanned area, dye accumulation within regions of the cell and the desired voltage driven signal effects all result in a similar response by the cell. These factors

present sources of ambiguity regarding changes occurring in a spectrum and render interpretation of these spectra difficult.

The sixteen period stacks proved to take the longest time for dye infiltration but were exhibited better maximal reflectance than 8 period films. I chose a middle ground of 12.5 period films beginning and ending with a high index dense layer. Larger area 18 mm  $\times$  25 mm devices were fabricated to permit lateral shifting of the cell before scanning if a bubble was created during the dye infiltration process.

Voltages in excess of 1000 mV produced excellent switching but also appeared to cause electrochemical dye breakdown. Such changes would lead to ion formation within the device (contributing to short circuits) or a change in cell electrical conductivity which would introduce new dye molecule transport mechanisms. The increase in system complexity associated with this behaviour was unacceptable.

### **3.5 Second generation device performance**

Twelve and a half period photonic crystals were deposited by GLAD for second generation devices using the same process parameters as previous depositions but employing a different motion control algorithm. The bandgap of these films was intentionally slightly misaligned from the absorption peak of methylene blue to prevent the entire spectrum shifting when dye

is shifted through the device. The shift to 12.5 period films and the moving of the bandgap center wavelength required the use of a 221 nm design structural periodicity to center the bandgap at 725 nm, moving the dye absorption peak to the band edge.

The inclusion of strips of 3M Magic Tape was used to create a uniform air gap of 44  $\mu\text{m}$  between the photonic crystal and the counter electrode. Further, cell assembly was performed in a class 1000 cleanroom to maximize uniformity in gap creation. Addressing voltages were restricted to less than 1.5 V ( $3 V_{pp}$ ) to promote longer device lifetimes.

The spectra that contribute to the cell's optical response are shown in Fig. 3.5. The switching phenomenon occurs in the wavelength range where there is overlap between the photonic crystal bandgap and a region of methylene blue absorption. The approximate wavelength range of the central bandgap of the  $\text{TiO}_2$  Bragg stack infiltrated with methanol is from 670 nm to 780 nm and methylene blue's primary absorption spectrum occurs from wavelengths 525 nm through 770 nm. The absorption strength of methylene blue decreases with increasing wavelength from its peak near 655 nm. While this bandgap alignment is not necessarily optimized for the highest reflectance switching performance, this photonic crystal periodicity exhibits a complete range of dye absorptive power within the optical bandgap. Across the wavelength range of the optical bandgap, maximal (complete reflectance suppression at short wavelength band-edge) and min-

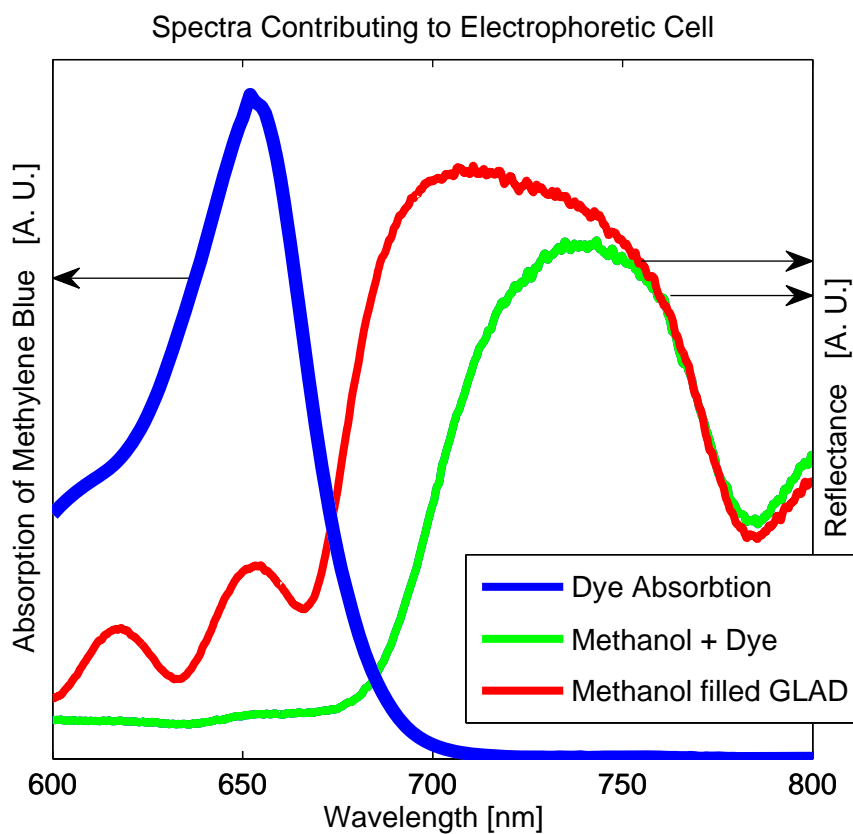


**Figure 3.5:** The three spectra of interest are displayed. In blue the absorption spectrum of a solution of methylene blue dye in methanol is shown. In red and green, the reflectance spectrum of assembled cells are shown, the red line indicates the bandgap when filled with plain methanol, and the green line when filled with a concentrated methylene blue solution. Arbitrary scale for all curves due to poorly quantified beam intensity (absorption) and poorly aligned reflectance apparatus (reflectance).

imal (no reflectance suppression at long wavelength band-edge) absorptive power are seen. These devices are then well suited to investigating and quantifying performance.

The quantity of methylene blue present within the Bragg stack is sufficient to extinguish nearly all reflection within the range of 670 nm at the beginning of the optical bandgap through to 685 nm. Partial reflection reduction is seen over the range of 685 nm through 760 nm. Above this range the relative absorptive power of the methylene blue dye at the dosage present within the cell is too weak to affect the optical properties of the cell. The wavelength range of this partial reduction is the domain of interest, and it is where a switching phenomenon may be created.

Spectra from one second generation device are shown in Fig. 3.6. The observed switching magnitude is seen to display competition between two different phenomena. The first is a saturation of absorptive properties, since the number of dye ions that have been infiltrated into the cell is observed to absorb and scatter all incident light at wavelengths less than 685 nm. The saturated dye solution used contributes a maximal number of dye molecules to the cell. Noting that the absorption of methylene blue in a methanol solution at 685 nm is approximately one tenth of its peak absorption near 655 nm, it may be surmised that the cell contains significantly more methylene blue molecules than would be required to extinguish the signal by methylene blue absorption where it is strongest. The competing element is that

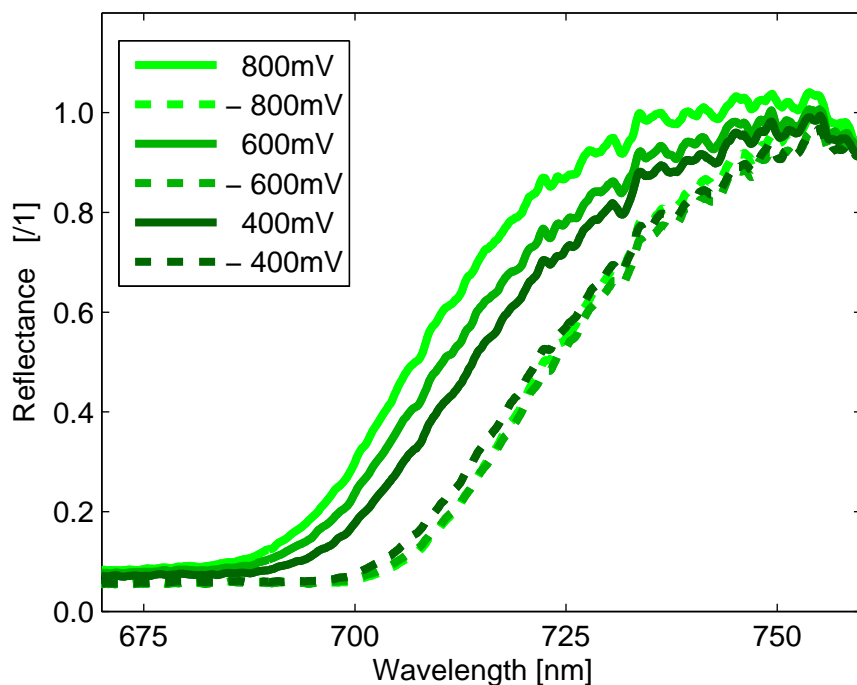


**Figure 3.6:** Reflectance Spectra achieved when driving the cell with 800 mV, 600 mV, and 400 mV. Negative polarity yields a reflectance minimum, whereas positive polarity drives dye out of the crystal for a reflectance maximum.

the component of the cell that drives the optical change is the absorption of these molecules, and these species' motion through the cell is critical to causing the optical change and hence their presence in larger quantities has greater potential to generate a strong optical response. Working with the saturated solution was qualitatively noted to provide a stronger response than a solution diluted to only minimally extinguish the signal.

### 3.5.1 Improved optical control

The device to device repeatability remains imperfect in second generation devices, but individual device performance was drastically improved by the changes made to the fabrication process. Device lifetimes were extended indefinitely by the combination of including spacers and an upper bound on the addressing voltage. No bulk drift is detectable in these devices after the first two minutes when the dye has settled into the photonic crystal and the reservoir. This facilitated recording significant amounts of data from second generation devices at various voltages for long durations.

The change observed in the reflectance spectrum with this bandgap configuration may be compared to a shift in the edge wavelength of the bandgap. While the interaction that gives rise to this change is different, the observed effect at the short wavelength band edge is analogous to the bandgap being shifted. This change is similar to the effect seen when a flexible photonic crystal is mechanically deformed and the optical path length increases slightly by stretching. This phenomenon is quantified by obtaining the spectra of limiting states in the switching process, ie: addressing voltages in 200 mV increments from 200 mV through 1200 mV. Applying a positive voltage to the front electrode shifts the band edge to shorter wavelengths. With a change in polarity of the applied field the band-edge is driven back towards longer wavelengths. Measured at 50 percent reflection

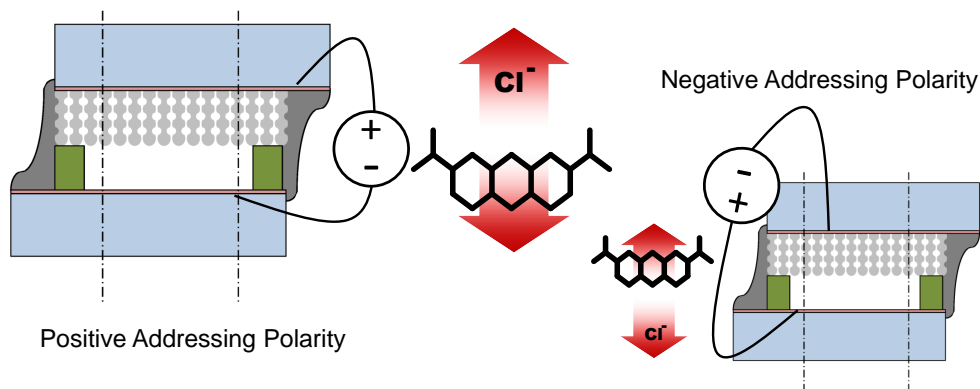


**Figure 3.7:** At left the positive addressing polarity and the corresponding dye motion are shown. At right, the negative polarity causes the opposite response.

we observe shifts of approximately 16 nm for cells driven by voltages of 800 mV and 1000 mV, 13 nm for 600 mV, 8 nm for 400 mV, and no measurable change for 200 mV.

This phenomenon agrees with all of the trends predicted by the mechanism described earlier. A potential gradient across the Bragg Stack and dye reservoir is created when a positive voltage is applied to the electrode that has the photonic crystal on it (top electrode in Fig. 3.1) with respect to the counter electrode as in Fig. 3.7. In the presence of this gradient the absorbing cations move away from the photonic crystal and towards the dye reservoir. Sufficient cations are displaced by this field that a decrease in the dye absorption and scattering within the photonic crystal occurs. Upon reversal of this voltage, the chloride ions in turn are repelled from the photonic crystal and the cations re-enter the pores in the  $\text{TiO}_2$ . The properties of the cell are

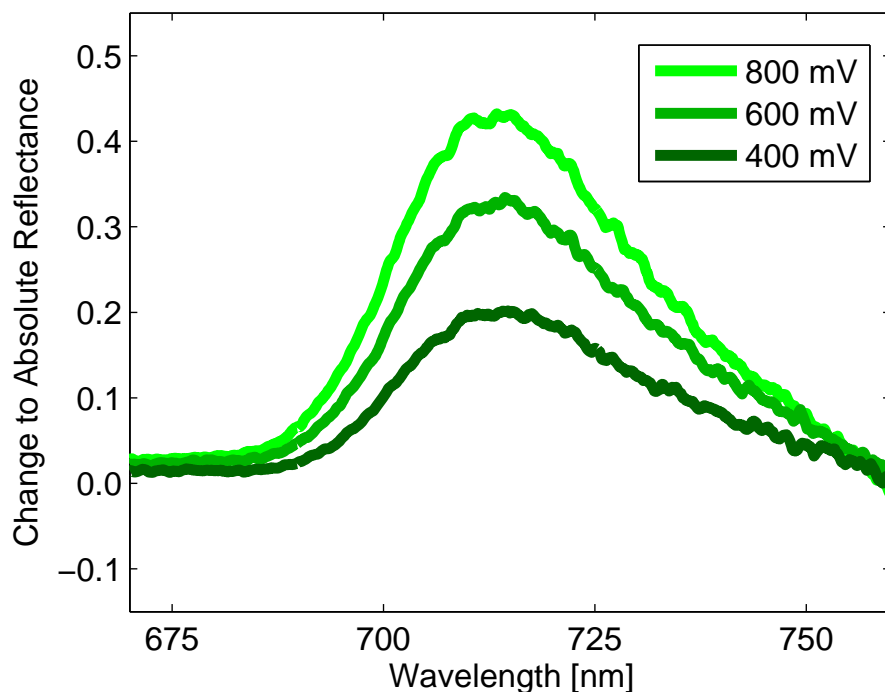


**Figure 3.8:** Three sample switching ranges are displayed (noise smoothed) with different voltages applied to the cell. These ranges represent the difference between spectra of positive and negative polarity. Polarity is measured as the voltage of the photonic-crystal-coated electrode with respect to the counter electrode (See Fig. 3.1 for schematic).

driven back to be comparable with those of the unaddressed state.

Fig. 3.8 displays strengthening of switching response over the voltage range of 400 mV to 800 mV. Stronger potentials display an increased dye molecule displacement from the photonic crystal. Further increasing the applied voltage from 800 mV yields no additional response, and increases beyond this result in electrochemical activity in the cell.

### 3.6 Summary

Devices were designed and fabricated permitting an interplay between dye absorption and the reflectance of a one dimensional Bragg stack photonic crystal's reflectance properties. A custom reflectance measurement apparatus was designed and assembled to monitor device performance. Both the reflectance measurement scheme and photonic crystal cell fabrication methods were improved by identifying areas giving rise to uncertainty in first generation cells. Second generation devices displayed a predictable and uniform reflectance response with applied voltages of less than 1000 mV. Switching contrast between reflecting and absorbing cell states was strengthened with increases in applied voltage between 400 mV and 800 mV and a maximal reflectance variation of 0.4 was achieved.

## CHAPTER 4

# TIME RESPONSE OF THE SWITCHING CELL

### 4.1 Introduction

The modifications made to the first generation devices outlined in Chapter 3 successfully improved device-to-device repeatability. Unfortunately, they introduced a significant reduction of the system's response time. This chapter<sup>1</sup> explores phenomenon that are revealed by the reduced response time. While not an advantageous development with regard to the device's performance metrics for application, such as a photonic crystal display, this investigation revealed information about the dye movement and processes governing light interaction within the photonic crystal bandgap.

First generation cells' responses were faster than the 100 ms spectrophotometer integration period (Fig. 3.4). It is reasonable to believe that were

---

<sup>1</sup>A version of this chapter has been published. Krabbe 2010, Applied Physics Letters. 97:041117. [77]

a great deal of effort and time invested in the manufacturing process to achieve uniform electrode separations and defect free films, the reliability seen in second generation devices might be maintained and response times similar to those observed with first generation devices may be recovered. The longer response times are a consequence of lower electric field strength caused by increased inter-electrode spacing and decreased driving voltage. This work presented in this chapter is explorative rather than developmental with regards to device performance. The slow response is instructive in a way that a rapidly responding cell measured by this apparatus is not: these devices afford a view into the inner workings of the electrophoretic switching process.

## 4.2 Response times

As in Section 3.4, the second generation photonic crystal devices were driven by a square wave voltage signal. The spectrum was monitored with the same spectrometer used in the previous chapter. However, a 30 ms integration period was employed replacing the 100 ms integration period used earlier. The trade-off in accuracy while measuring instantaneous signal strength benefits the speed at which spectra may be recorded. By approximately doubling the uncertainty in measurement to 4%, a tripling of the time-resolved precision was gained.

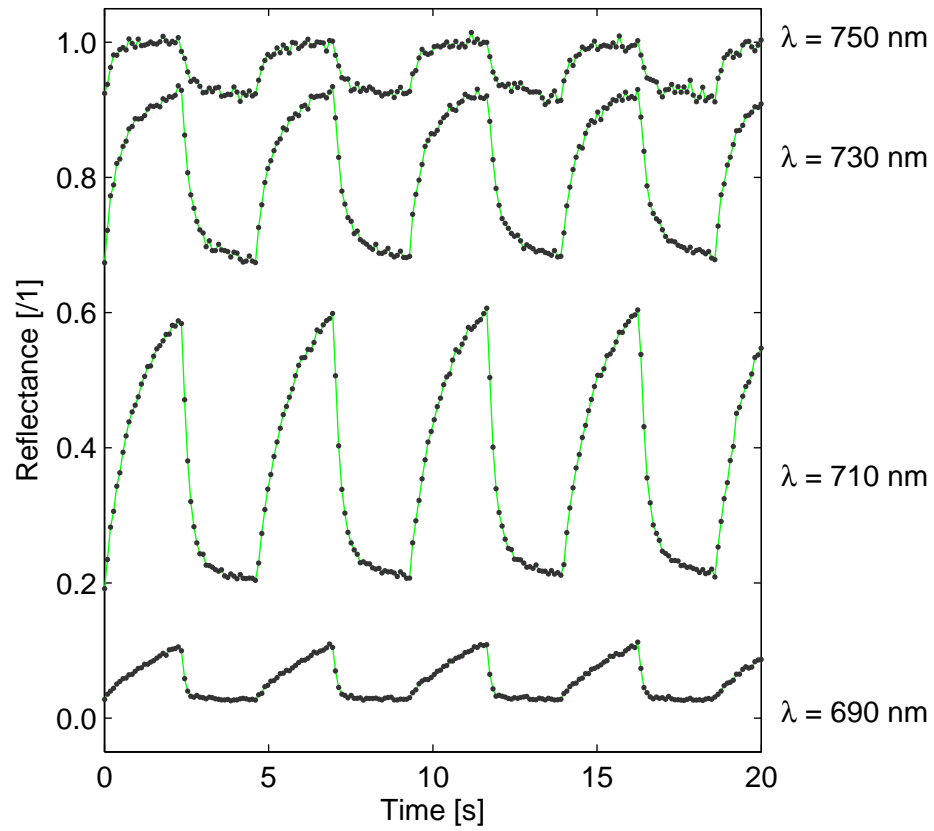


**Figure 4.1:** Time responses of a cell shown at four different wavelengths when driven at 1000 mV.

The optical response at four different wavelengths across the region of interest in the second generation switching cells is displayed in Fig. 4.1. The sharp response to the square wave switch (especially from the time series displayed at  $\lambda = 710$  nm) indicates that the dye starts movement within less than 30 ms of the signal generator's switch. Furthermore, the change in exponential response of reflectance with wavelength (next section) is evidence that circuit capacitance or inductance do not play a major role. This observation permits using the optical response signal as an indication of the voltage square wave driving signal's turning points and frequency.

#### 4.2.1 Quantifying the time response

To quantify the device response time, exponential curves were fit to the data shown in Fig. 4.1. Doing this necessitates numerically identifying the turning points in the response's switching. Performing this manually is straightforward but unrealistically tedious so the task is done automatically by low pass filtering the time response. One simple discrete time low pass filter implementation is equivalent to an exponentially weighted moving average, and implementing a low pass filter based on only the positive-frequencies (a trailing moving average), was very accurate in determining the turning points. Setting the filter with a low-pass frequency equivalent to that of the switching signal performed the task reasonably well for wavelengths that exhibited some switching response, and nearly perfectly (compared with

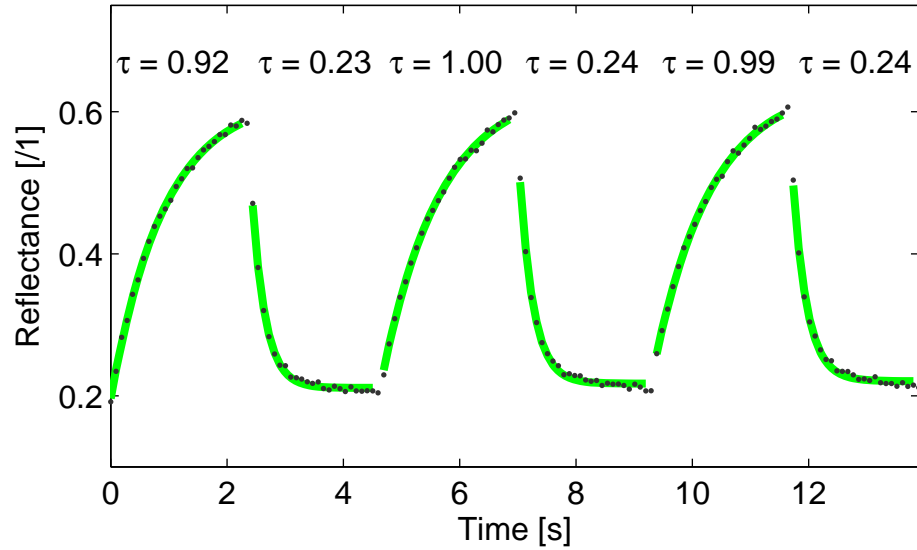


**Figure 4.2:** A time response for a cell driven at 1000 mV as shown in Fig. 4.1 for  $\lambda = 710$  nm with exponential fit curves and calculated time constants shown for reference.

manually selected turning points) for wavelengths near the strongest response at  $\lambda = 715$  nm. The calculations for this wavelength of light were used to snip the exponential response time series data for all wavelengths. These individual time responses were matched to a least-squares fit of a simple first order exponential (Eq. 4.1) and the time constants were measured. The parameter  $I_{\infty}$  is the eventual steady state reflectance that would be reached after a very long settling time and  $I_0$  scales with the deviation of the signal from this intensity at the time  $t_{turning\ point}$  when the signal begins to switch.  $\tau$  is the parameter of interest and is the first order exponential response's characteristic time. A sample of fits performed on the data in Fig. 4.1 is shown in Fig. 4.2.

$$I(t) = I_0 \times e^{\left(\frac{t-t_{\text{turning point}}}{\tau}\right)} + I_\infty \quad (4.1)$$

Time constants extracted from these exponentially varying response curves are displayed for wavelengths spanning the domain of interest in Fig. 4.3. On occasion the exponential fit to the data during this batch processing fails. A typical reason for this is when noise perturbations affect a few early datapoints in a time series. The least-squares fit's sensitivity is more heavily reliant on the first datapoints in the exponential decay, and so noise in recording here is particularly detrimental. Poor fits are eliminated based on comparing the time constant calculated to the bulk body of data using Chauvenet's criterion [78] called recursively. The time constants presented for each wavelength result from fitting to 20 cell switching periods and accepting data and averaging it where the fit is calculated to be statistically reliable.

The three curves presented in Fig. 4.3 represent different driving voltages. Their similarity indicated that the cell's response speed is not voltage controlled, but rather governed by species mobility through the photonic crystal's pores. The larger reflectance switching ranges seen at higher voltages (see Fig. 3.8) are concurrently achieved, meaning the instantaneous rate of change of reflectance does vary while the time constant of the shift does not. The unusual behaviour of a change in response time with  $\lambda$  is

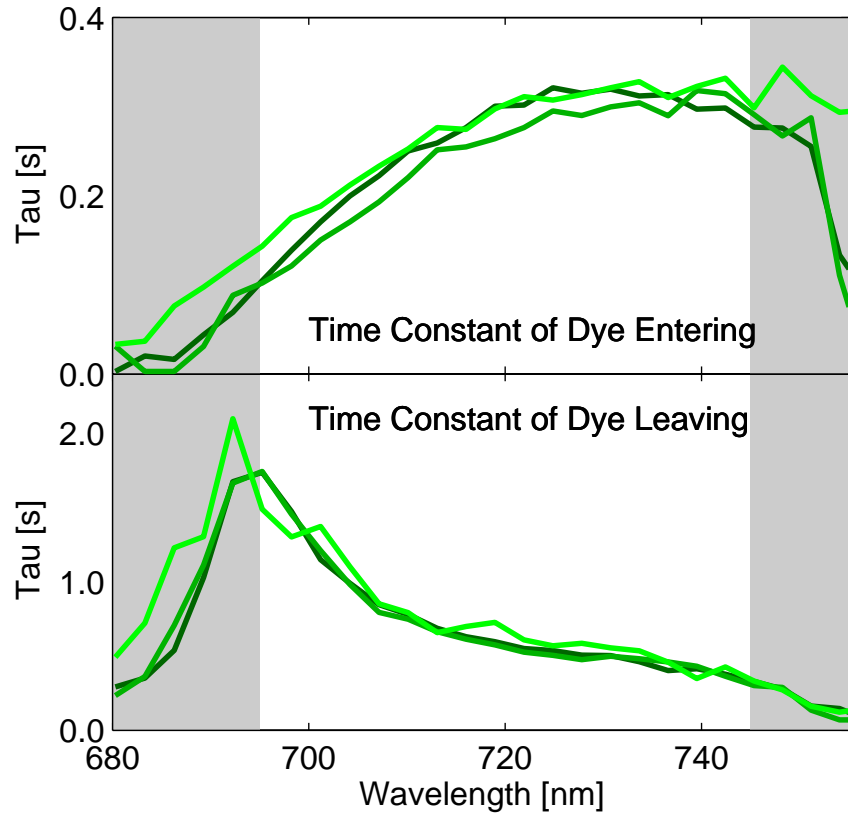


**Figure 4.3:** The calculated characteristic time constants of the optical response. Driving voltages of 600 mV, 800 mV, 1000 mV are shown in light, medium and dark green respectively. Gray borders indicate wavelengths where rise or fall behavior resembled a clipped exponential.

addressed in the next section.

Outside 695 nm - 745 nm the optical response follows a clipped exponential profile. These truncations in optical change appear to occur when dye concentration varies beyond the necessary threshold for extinguishing the signal or when a maximum in photonic crystal reflectance is reached. This type of optical response is visible in the  $\lambda = 690$  nm and  $\lambda = 750$  nm response curves of Fig. 4.1. The fast time constants in this region are the result of a fit to non-exponential behaviour, and do not accurately describe the dye migration.

Inspection of Fig. 4.3 shows that for all wavelengths between 695 nm and 745 nm reductions in reflectance (dye entering the photonic crystal) occur faster than increases in reflectance. This hysteresis may be attributed to the photonic crystal's porous nanostructure. GLAD TiO<sub>2</sub> structures are known to exhibit a distribution of pore sizes. While large pores exist between the columnar microstructures seen in Fig. 2.4, a smaller scale porosity occurs within the columns themselves [79]. The nanostructure's extremely large surface area, due to these mesopores, acts as an adsorption sink for methylene blue which is known to adsorb on titania [80]. Dye redistribution amongst varied size pores occurs on scales significantly shorter than  $\lambda$  meaning that the bulk optical properties should not be susceptible to inter-pore dye settling.

Dye ion mobility in the large and well connected pores is greater than

that in smaller pores due to larger cross sectional areas of the channels [81,82]. This configuration permits fast dye ion inflow to the photonic crystal structure. However, when the applied field drives ions from the photonic crystal, the dye which has since migrated into small pore networks is subject to the rate limiting slow desorption time, slowing the overall optical response time for dye outflow.

#### **4.2.2 Modelling the wavelength dependence of optical response times**

Wavelength dependence is observed within the photonic crystal's optical response times. The dye's absorption properties are based on dye concentration and, independent of other optical phenomenon, these properties are expected to change uniformly at all wavelengths. Dye absorption may be stronger at one wavelength than another but this results in an increasing change in magnitude rather than an increased rate of change in the optical response. Wavelength dependence is not predicted to occur for variations arising strictly from dye distribution. This unique phenomenon's presence suggests that the photonic crystal's interaction with light is facilitating a change in the device sensitivity to dye at some wavelengths.

It is believed that the switching speed's wavelength dependence results predominantly from a change in the group velocity of light within the photonic crystal. Gain or loss mechanisms encountered by photons interacting

with the photonic crystal are magnified by such a group velocity slowing, especially near the band-edge [83]. Modeling this effect for the photonic crystal structure of the 12.5 period  $\text{TiO}_2$  photonic crystals developed for the second generation devices was done using a plane wave approach based on transfer matrices [13].

The indices of refraction for the various layers of the film were modelled by a two term Cauchy dispersion relation [84]. In addition to this real component of the index of refraction a positive imaginary component was added. The imaginary component of refractive index models the light's interaction with a normally behaving absorber, or one described according to the Beer-Lambert Law [85]. This description of methylene blue absorbance is accurate when presuming that the absorbing molecules act independently of one another, and that the dye was considered to be homogeneously distributed within each layer of the Bragg Stack. Additionally the incident light was treated as travelling only perpendicular to the photonic crystal structure and so the light evenly interacts with the absorbers and it was presumed to be of sufficiently low intensity to have negligible effect on the absorber populations in the ground state (optical pumping did not occur). By standard conventions, a positive imaginary component of a material's index of refraction interacts with the imaginary component of a phasor describing a beam of light and resulted in an exponentially decreasing amplitude with propagation.

To model a uniform absorber that has equal absorption at all wavelengths, the complex component of the index of refraction must be proportional to wavelength. A range of uniform absorber concentrations are modelled within a 1  $\mu\text{m}$  thick slab. The complex indices of refraction of these various absorber concentrations are shown in Fig. 4.4a at top. The corresponding transmission through the 1  $\mu\text{m}$  thick slab is shown at bottom and is constant across all wavelengths.

Modelling a hypothetical dye with no wavelength dependence in absorbance would be useful to relate observed absorption of the dye to effects of the photonic crystal. Modelling the absorption spectrum of methylene blue was also necessary to correlate this data to spectra measured from the photonic crystal devices. This was done by creating a complex index of refraction profile within another 1  $\mu\text{m}$  slab that corresponds to the absorption spectrum of methylene blue. The shape of the absorption spectrum was simulated by a sum of two Gaussians centered at 617 nm and 654 nm with amplitudes and widths chosen to replicate a measured methylene blue absorption spectrum in plain methanol. The result of this approximation is seen in Fig. 4.4b at top. At the bottom Fig. 4.4b shows the transmission properties of the modelled slab of methylene blue dye in a hypothetical solvent with  $n=1$ .

The straight set of seven lines representative of the uniform absorber (Fig. 4.4a) have equal magnitude at a wavelength of 690 nm to the curved

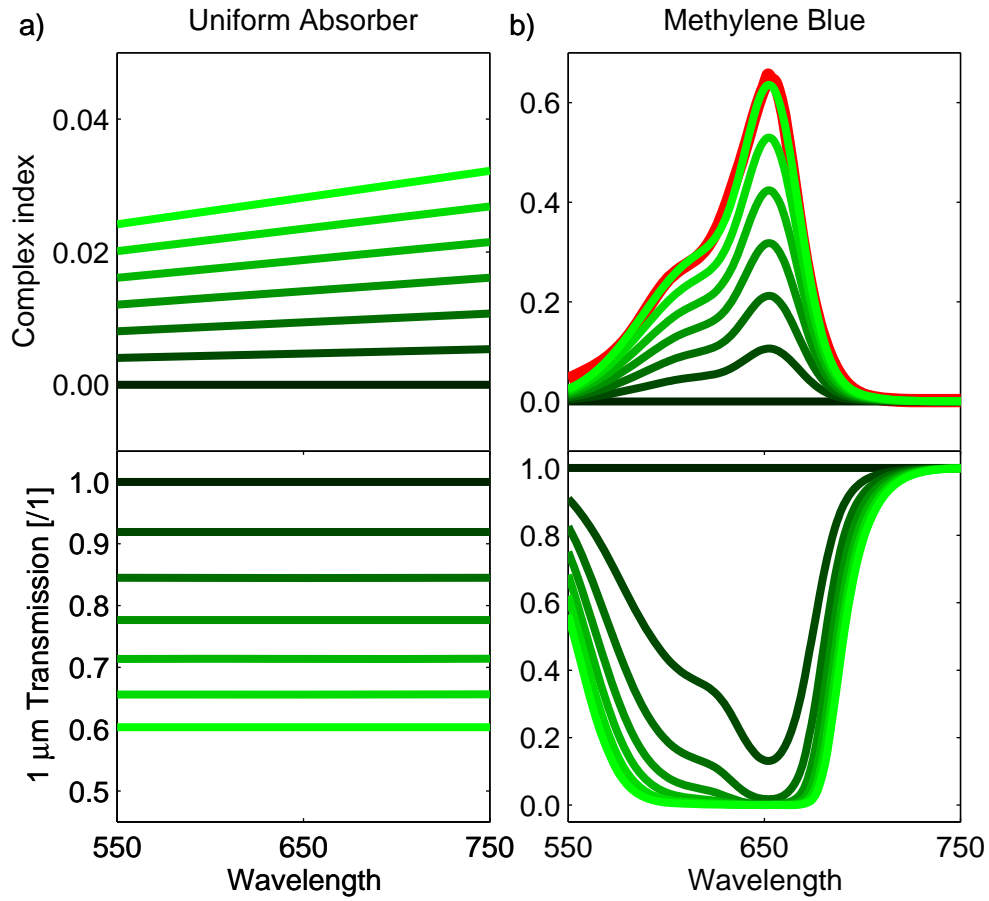


**Figure 4.4:** a) Top - Complex component of index of refraction used to model a uniform absorber as a function of wavelength. Bottom - Transmission spectrum of a  $1 \mu\text{m}$  thick slab of this absorber. b) Top - Complex component of index of refraction used to model methylene blue as a function of wavelength. The spectrum is composed of two gaussian curves centered at 617 and 654 nm and matched to fit an experimentally measured absorption spectrum seen in red. Bottom - Transmission spectrum of a  $1 \mu\text{m}$  thick slab of methylene blue solution (in hypothetical solvent with  $n=1$ ).

set of lines representative of the absorption characteristics of methylene blue (Fig. 4.4b). The magnitude of the complex index of refraction is not calibrated to the physical dye concentration present in the electrophoretic cells but by matching the uniform absorber to an absorber representative of methylene blue the correlation may be drawn between pairs of modelled spectra. This permits a form of cross calibration between models when comparing measured spectra without determining an absolute quantitative measure of dye concentrations.

The numerical model of the photonic crystal made use of  $2 \times 2$  transfer matrices which were calculated for each layer and then multiplied with one another according to the standard formalism yielding the transfer matrix of the whole system. The entire modelled device's optical properties were then extracted from the values of the system transfer matrix [13]. These calculations were performed for all wavelengths of interest. The parameters were refined to describe the film microstructure by manually iterating selection of both the indices of refraction and the device periodicity to match the shape of the measured optical bandgap reflectance spectrum.

When absorbers are introduced into the model using a complex index of refraction, light was presumed to be lost from the model by describing absorbance in this manner. The loss of light is an inaccurate representation of reality, but an accurate description when modelling the normal incidence reflection and transmission. Collimated light propagates through no solid

angle while the fluorescence of an absorber would be distributed evenly across all  $4\pi$  steradians, and so, photon re-emission can be assumed to be undetectable in a reflectance measurement.

The reflectance response of a 12.5 period Bragg stack is modelled in Fig. 4.5 with the presence of uniform absorbers. The change between successive lines occurs as the uniform absorber is introduced to the photonic crystal in increasing quantity. At bottom, the photonic crystal's reflectance was shown to decrease as the quantity of absorber (representative of dye concentration) increases. At top, the corresponding colours indicate the relative absorption strength at different wavelengths. The system's absorption strength was quantified as the light intensity removed from the reflectance and transmittance spectra, indicative of it being absorbed. Absorption strength (per unit of the absorber) was significantly greater near the bandgap edges. This was the effect one would predict based on the group-velocity slowing of photons occurring at those wavelengths. For comparison, in the absence of a photonic crystal, these absorption strength spectra are flat as in Fig. 4.4a at bottom.

Increasing the quantity of absorber present in the device monotonically increases the absorption strength at all wavelengths inside and outside the bandgap. Fig. 4.5 shows absorption relative strength normalized to the absorber strength at the bandgap center. This is a representative measure of the optical effect per unit of absorber added to the photonic crystal.

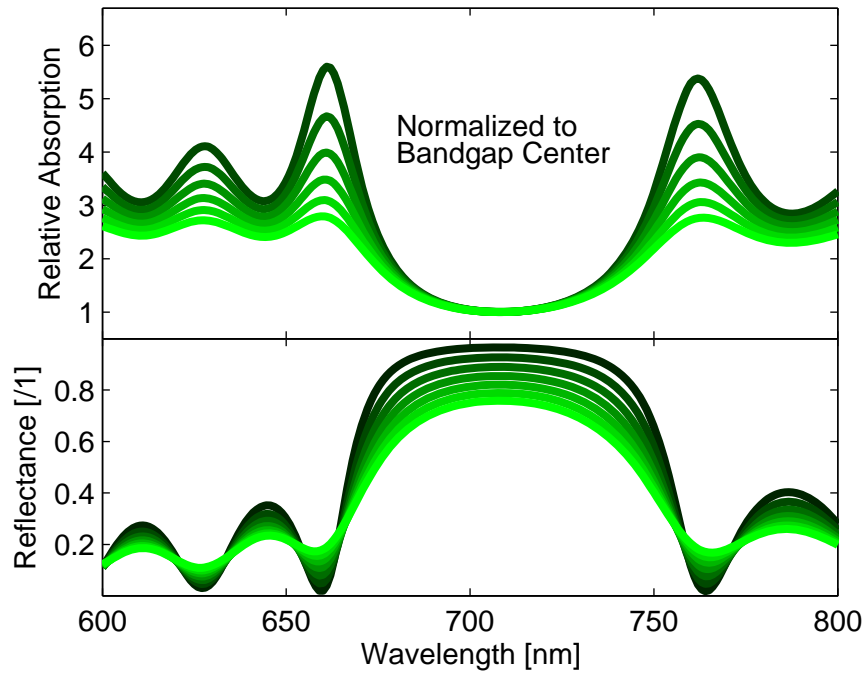


**Figure 4.5:** At bottom, the reflectance response of a photonic crystal is displayed with a range in concentrations of a uniform absorbing species (Fig. 4.4a) added to the device. Black represents a low absorber concentration and green a high absorber concentration. At top, the absorption strength quantified as amount of light removed from transmittance and reflectance spectra is calculated and normalized to the strength at bandgap center wavelengths.

The uniform absorber used for calculation of Fig. 4.5 was replaced by the spectrally specific description of methylene blue (Fig. 4.4b). Doing this resulted in a calculation displayed in Fig. 4.6. These coloured curves may be matched with those in the inset to confirm that the general response due to methylene blue infiltration was plausibly represented. If the modelled reflectance was compared to that measured during the device operation, the corresponding dye molecule concentrations may be related to the uniform absorber effects according to the relationship established in Fig. 4.4. The calibration to the lowest curve (representative of the highest dye concentration) in Fig. 4.6 results in a feasible band-edge absorption enhancement of close to two times that seen at band-center wavelengths (as per Fig. 4.5). From these measurements it can be hypothesized that the band-edge response times could be approximately two times faster or slower than that seen near the band-center. This was indeed the order of magnitude enhancement observed in Fig. 4.3.

The trend observed in Fig. 4.5 additionally demonstrates that the first absorber introductions (initial dye infiltration) has greater effect, per unit dye concentration, than later additions of dye. The device's response sensitivity at band-edge wavelengths is greatest for the lowest dye concentrations. Relative to mid-bandgap wavelengths, near the short wavelength bandgap edge the reflectance is expected to respond more rapidly to small increments in dye during inflow and require more complete dye removal during outflow,

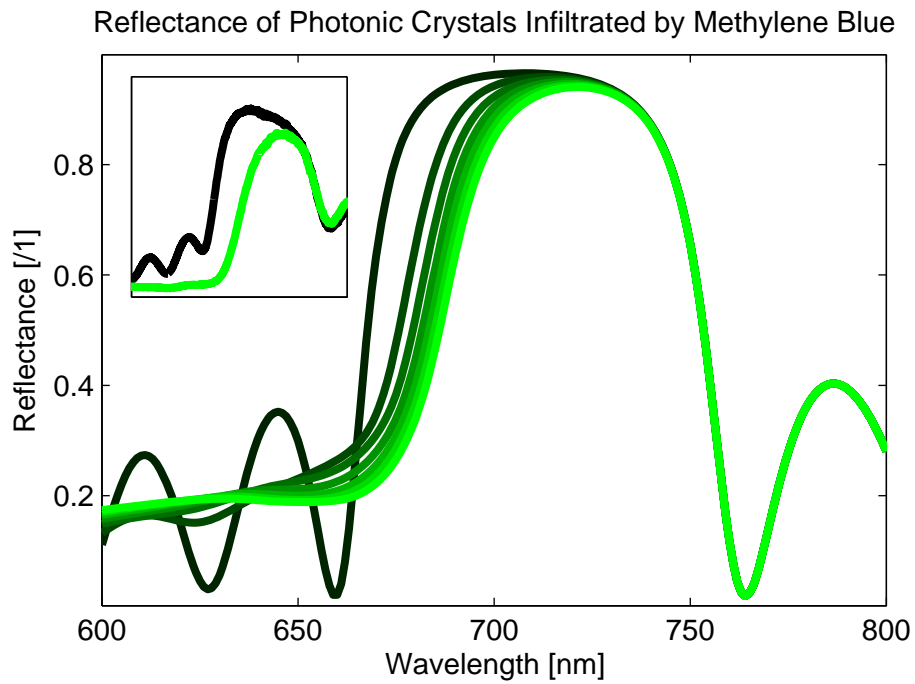


**Figure 4.6:** Simulated spectrum of a  $\text{TiO}_2$  photonic crystal with increasing concentration of methylene blue, changing colours are roughly equivalent to the quantity of absorber denoted in Fig. 4.5 according to the relationship established in Fig. 4.4. Inset indicates the experimental relationship over the same wavelength domain as was detailed in Fig. 3.5.

these are exactly the trends seen in Fig. 4.3.

### 4.3 Summary

The changes made to improve device reliability increased the photonic crystal device response time. This afforded an opportunity to closely examine the phenomenon underlying these cells' optical behaviour. First-order exponential fits were made to time-series recorded data from cells undergoing switching. The resulting time constants displayed hysteresis in dye motion likely due to GLAD film porosity. A wavelength dependence in response time was also observed, and this was plausibly attributed to changes in group velocity due to the photonic crystal bandgap. Modelling the photonic crystal structure with an absorbing species indicates that the explanations made for these effects are on the right order of magnitude. The correlation of this static model's results to the dynamic dye flow processes are reasonable however this does not rule out the possibility of other phenomenon contributing to the wavelength dependence observed in the device's behaviour.

## CHAPTER 5

# 3D PHOTONIC CRYSTALS

### 5.1 Introduction

The 3D photonic crystal structure proposed by O. Toader and S. John in 2001 [36] precisely specified the square spiral structure that would produce an excellent complete photonic bandgap. The diamond:1 structure is based on the diamond lattice structure and is [55] a square spiral lattice connecting the diamond lattice's first-nearest neighbours by successive spiral arms of the microstructure. Neighbouring spirals spaced in a two dimensional array trace out a path through neighbouring lattice points together reaching all the lattice points in each diamond unit cell. The diamond:5 structure, connecting 5<sup>th</sup> nearest neighbour lattice sites, promises theoretically superior optical characteristics but poses a greater fabrication challenge due to the required angles of the arms. Initially the diamond:1 architecture was fabri-

cated in silicon using GLAD [50] in a rough approximation to the optimal geometry.

Much work has been done on optimizing and investigating the performance of silicon diamond:1 square spirals [43,51,52,54,86]. The deposition algorithms for attempting to fabricate the optimal structure are readily available. The decision to work with silicon and air was made for a number of reasons. Because of silicon's very high index of refraction, the large contrast that it exhibited against a vacuum or air background allowed for wider tolerance in matching the idealized geometry during fabrication. Additionally, properties of silicon deposited using an electron beam evaporator with GLAD were favourable. One obstacle in trying new square spiral fabrication methods based on other materials and for other wavelengths has been the fabrication of the seeding layer upon which the films could be deposited. These layers require significant fabrication effort and time. Optical wavelength square spiral photonic crystals have not yet been attempted, partly due to the obstacle of fabricating a narrower lattice of seeds and partly due to the fact that silicon, the workhorse material for all square spiral photonic crystals up until this point in time, has very poor transmission properties at optical wavelengths.

When O. Toader and S. John published a more complete investigation of the geometry [55] in 2002, the architecture's tolerances were provided to the scientific community to decide what could work and what simply wouldn't

when it came to fabricating square spiral photonic crystals. Any substance possessing an index of refraction in excess of  $n=2.2$  could be used, including Si and  $\text{TiO}_2$ . While the tolerances associated with architecture optimization would be tighter than when working with silicon,  $\text{TiO}_2$  is a candidate for creation of 3D photonic crystals. The anatase crystal structure may be formed using GLAD posts when they are subject to post deposition annealing [79], but the rutile phase is not ruled out. The indices of refraction of these crystal structures (anatase  $n=2.5$ , rutile  $n=2.7$  [87]) yield potential complete photonic bandgaps in the 5-8% range if fabricated into an optimized diamond:1 square spiral.

Fabricating a 3D square spiral switching cell infiltrated with methanol and a laser dye may be possible, but a complete photonic bandgap is a physically impossible target. Even at its most optimized, the index contrast lost when replacing the air voids with methanol filled voids prevents formation of anything more than a pseudobandgap. Despite lacking the potential for replicating the one dimensional photonic bandgap modulation within a three dimensional photonic bandgap using the method described in Chapters 3 & 4, the decision was made to pursue fabricating a visible wavelength square spiral photonic crystal in  $\text{TiO}_2$  as a parallel but independent project.

### 5.1.1 Effect of seeding on film morphology

Films deposited by GLAD result in stochastically ordered post distributions when the deposition takes place onto a planar substrate. In such a situation nucleation takes place randomly, as the first incident particles from the vapour flux land on the surface. In early post growth in a GLAD film the nuclei on the surface compete to collect incident particles as they shadow one another. As these posts grow the stochastic nature of the incident flux means that some posts will grow slightly faster, thicker, or taller than the surrounding columns. While the fluctuations may initially be small, these perturbations exaggerate themselves. Thicker and taller posts will broaden and grow while neighbouring posts may be completely shadowed and their growth totally extinguished [88].

The position of GLAD columns may be controlled by patterning physical bumps to preferentially nucleate growth of columns. Two important features will result if the seeds are appropriately sized and spaced. First, GLAD film growth occurs on those bumps and the 2D seed/column pattern on the substrate surface is maintained as the film thickness increases. Thus, a two-dimensional periodicity on the surface will result in a two dimensional periodicity in the film. The second feature that occurs is slightly less obvious but similarly important. A specific combination of seed spacing and vapour flux incidence angle  $\alpha$  results in column growth with well

defined and specific size. The consequences of seeding and incidence angle in all geometrical combinations results in a characteristic division of the incident flux according to a uniform pattern amongst growing columns. During growth periods when neighbouring columns are structurally very nearly identical the flux distribution amongst all growing columns is the same, and each post receives an incident flux shadowed by a number of the nearest columns. Eventually, if the film is grown to be thick enough, the vapour stream's stochastic nature will introduce fluctuations in post thickness and height. These variations alter the shape of the shadows cast across the substrate surface and the flux distributions become weighted in favour of further growing already marginally thicker and taller columns. As this process continues through the deposition it eventually leads to post broadening and post extinction [53].

GLAD growth on ideally seeded substrates typically results in film microstructures like the one shown in Fig. 5.1. Very different film morphologies result from seeded and unseeded substrates. Both the effects of seeding (controlled post location and controlled post shape) are clearly distinguishable between part a) and part b) in this figure. The seeded substrate shows that column placement occurs on raised bumps on a 320 nm square lattice on the substrate surface. Column broadening is far less rapid in Fig. 5.1b), especially within approximately the first 1  $\mu\text{m}$  of growth. While broadening does occur, the uniformity of post width through the full film thickness is

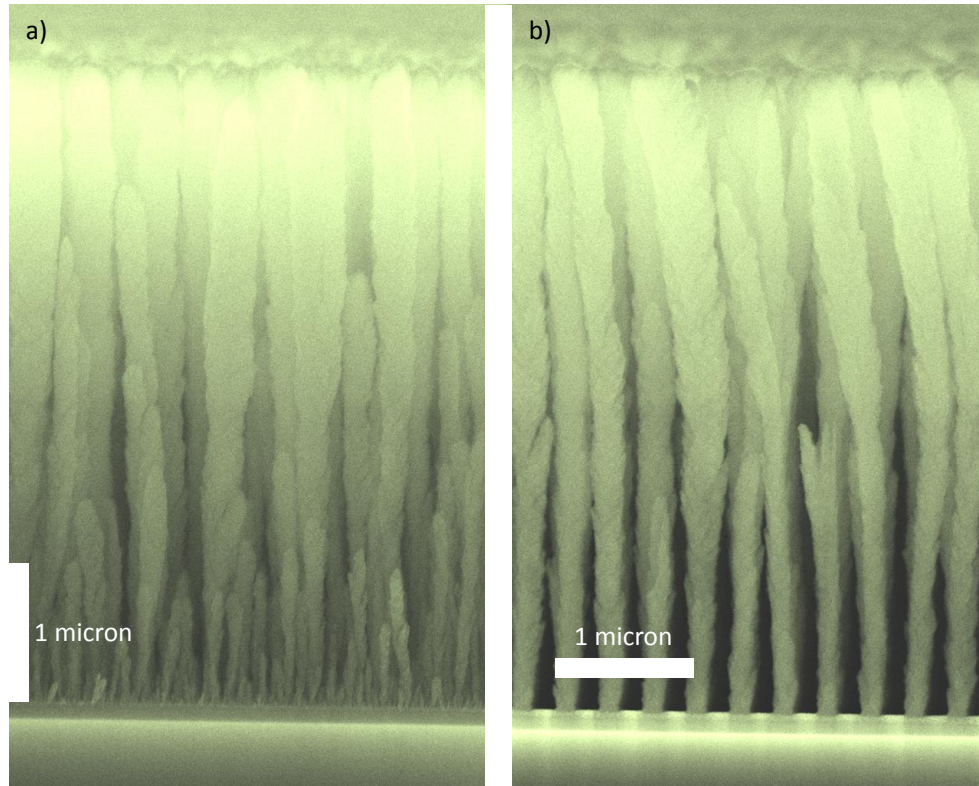


**Figure 5.1:** Comparison of seeded and unseeded GLAD growth of an SiO<sub>2</sub> film. a) displays the natural growth and column competition on a flat substrate and b) shows the column placement and column width selection caused by pre-patterning the substrate. Thanks to Steven Jim for including this seeded substrate in one of his depositions.

considerably improved. Column extinction within a film of set thickness, while not necessarily completely eliminated at very large film thicknesses, is greatly reduced (many extinct columns are visible along the bottom of Fig. 5.1b).

Both precise column placement and column thickness uniformity are required for fabricating high quality 3D square spiral photonic crystals. These stringent requirements pose a challenge for fabrication of these nanostructures by GLAD or other techniques.

### **5.1.2 Fabrication of seeded substrates for GLAD**

Several methods have previously been employed for fabricating the seeded substrates required for ordered GLAD film growth. An early method employed the use of a positive electron beam lithography resist which was used in concert with a lift-off technique to pattern seeds on a surface [89]. Negative resist electron beam lithography has also been used very successfully to do this work. The negative resist allows the seeds to be patterned directly in the resist and used as is, without a topography transfer process [43]. Eliminating a post-writing processing step allows the most direct control for pattern formation and is thus favourable when the direct writing is being used to produce multiple patterned substrates. Direct laser write lithography [90] has also been used to fabricate seed patterns but does not provide the same resolution as an electron beam lithography process due to focussing con-

straints. Colloidally aligned microsphere arrays can also be used to make patterned substrates, either by deposition onto the self-assembled particles or onto seeds lithographically patterned by a shadow mask of the colloidal array [91,92]. Colloidal assembly can be performed at full wafer scale [93], an enormous size compared with any nanoscale direct-write method. The array geometry for almost all self assembly methods is restricted to hexagonal closest packed (hcp) however, which is not compatible with optimized square spiral architectures. Block co-polymer patterning [67] is capable of forming similar hcp lattices on size scales between 10 nm and 200 nm nearest neighbour spacings [94]. Such seeding arrays may be formed over large areas much like colloidal self assembly. Both these large area patterning techniques however, present challenges in achieving defect free lattices over large areas, and the occurrence of lattice grain boundaries may be unacceptable in some devices.

These techniques may be categorized as either direct write, and therefore expensive in time and cost, or as self-assembled, and somewhat unwieldy in control. Situations in which both patterning techniques are applicable certainly exist, however neither is realistically an acceptable method for patterning substrates for large area square spiral photonic crystals where long range, precise and uniform seeding alignment is crucial and direct-writing cost is completely prohibitive.

## **5.2 Electron beam lithography fabrication of a nanoimprint lithography stamp**

By combining a replication method and a controlled direct write process it is possible to surpass the substrate patterning performance of both traditional direct write and self assembly methods. Nanoimprint lithography is a replication method that may be used in conjunction with a direct write technique. It reduces the need for patterning by a direct write method to a single occasion and then allows replications to be made using an imprinting process in significantly less time and with greatly reduced costs when compared to the direct write methods. The inverse topography must be fabricated by a direct write method. Electron beam lithography is capable of making such patterns and due to its accessibility in our research lab it was the method of choice.

### **5.2.1 Positive resist electron beam lithography**

The stamp topography required for fabricating seeding arrays for GLAD square spiral photonic crystal thin films is a square array of indentations. These indentations are filled with the nanoimprinting resist during replication resulting in a raised topography on the final substrate surface capable of nucleating growth. Fabricating these recessed areas is most easily performed using a positive resist with point exposure followed by developing

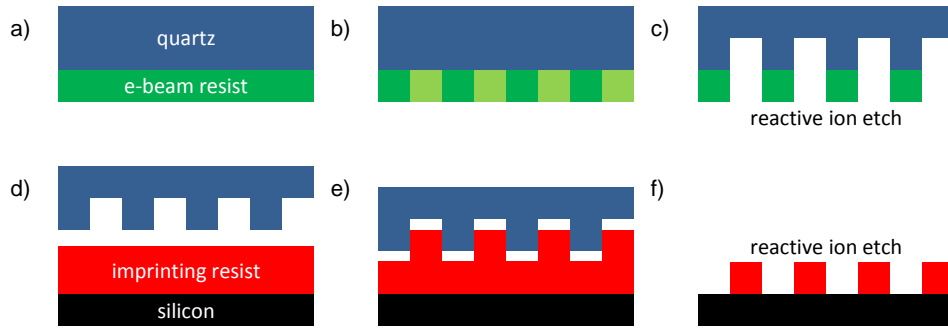


**Figure 5.2:** Process steps in fabrication of stamp and the subsequent thermal imprinting process. a) Electron beam lithography resist (PMMA) is spread of quartz substrates. b) Exposure of pattern perforates the resist which is subsequently developed. c) A reactive ion etch transfers the resist pattern into the quartz and is then cleaned away. d) Thermal imprinting resist (NXR-1025) is spread on silicon substrates. e) The resist is heated and imprinted by a nanoimprinter and the mould is released. f) (Optional step) The resist is thinned and hardened by a reactive ion etc creating the final seeds.

and a direct substrate etch through the resist mask. These steps are diagrammed in Fig. 5.2 a)-c).

Polymethyl methacrylate (PMMA) is the positive electron beam lithography resist most well documented and supported in the nanofabrication facility where this work was to be completed. It was selected for use, as the knowledge base surrounding its properties and behaviour within this fabrication facility were the best of all alternative options. PMMA is well characterized and has been widely used as a high resolution positive resist around the world for many decades since its first characterization in 1968 [95]. Significant improvements have occurred since. Various polymer weights have been well characterized and many subtle variations of PMMA are available, yielding finely tuned performance from products that are com-

mercially available. Exposing PMMA resists with electron beams has been well studied and the resolution limits are well understood [96]. This interaction has also been very successfully modelled [97, and references therein] and the key factors contributing to characterizing an exposure is well documented.

PMMA is broken down into lower molecular weight components by the electron beam interacting with the polymer and thus its solubility increases. The electrons' energy is delivered to the resist both directly (by electrons upon first interaction within the collimated beam), and indirectly (electrons that are backscattering from the substrate). The proportions of exposure energy due to direct penetration versus backscattering are a characteristic of the accelerating voltage which controls the electron energy, the electron beam focussing quality, and aperture size. These proportions depend on resist thickness and substrate composition as these parameters determine how the electron beam is dispersed upon impacting the surface.

The electron beam's interaction with the resist results in breaking of the polymer chains in the resist. The average molecular weight of the resist layer changes according to electron beam energy delivered by the exposure. Large doses (large number of electrons delivered to the resist) are patterned where the resist is to be removed and the regions where this occurs are considered to have been exposed. Designing an electron beam process that either fully exposes or completely unexposes the resist in any one spot is

difficult due to scattered electron interactions. Regions subject to high exposure doses result in a low average molecular weight (and high solubility within the developer) and regions subject to low exposure doses result in lesser reductions in molecular weight (and the solubility of the resist in a developer solution remains low). Ideally the developing conditions selected result in a high contrast between states of exposed and unexposed, ie: the developer dissolving all of the resist mask's regions that have received an electron dose greater than a specific threshold and the resist remains completely intact where the applied dose is below that threshold.

Electron beam exposure dose is the most easily and precisely controllable step in the process. By selecting a standard resist preparation, substrate, and developing procedure it is possible to determine the ideal exposure's pattern and strength by testing and iterating the exposure procedure. Convergence on reliable dose requirements for a certain pattern is highly likely. This is not true in limiting cases such as at the resist's resolution limit, or the electron beam's resolution limit. When realistic expectations are placed on the exposure and pattern requirements, dose refining is generally both straightforward and successful.

### **5.2.2 Determining an appropriate exposure dose**

Calculating the dose required to expose the lattice points in a 2D square array was desired for lattice spacings ranging from 80 nm through 400 nm.

The cleared area at each lattice point following resist development was circular due to the electron beam symmetry. Hole diameters equal to one quarter the lattice spacing were desired. This geometry leaves a robust resist layer intact following perforation where larger holes tended to yield a fragile mask for the etch process. The etch process is expected to isotropically undercut the resist mask yielding seed diameters larger than 25% of the lattice spacing and in the range of seed geometries previously shown to be optimal. Film morphology has been well studied for seeds at 33% of the lattice spacing [90] and the optimized seed width to minimize inter-seed deposition has been shown to be 50% of the lattice spacing [54] however the optimized square spiral geometry requires post diameters equal to 40% the lattice spacing [55]. Seeded columns that are too small may enlarge during deposition whereas seeded columns wider than optimal are likely to bifurcate as the column grows. Designing the exposure dose to yield resist holes of 25% the lattice spacing in diameter was hypothesized to be likely to yield seed widths somewhere between 25% and 40% of the lattice spacing that would be amenable to subsequent use.

Point doses suggested by the specification for the commercial resist being used were delivered spanning the range from zero through approximately 50 pA·s to square lattices across the desired range of lattice spacings. Sample results of these exposures can be seen in Fig. 5.3 where the following general trends are evident. Comparison of Fig. 5.3 a) and b) shows that the hole

size at any one lattice spacing increases with an increased delivered dose of current. Fig. 5.3 b) through f) display the required trend to maintain the hole width at approximately a quarter the lattice spacing. The dose required to increase the hole diameter increases at a rate that is faster than linearly proportional to the lattice spacing.

Measuring hole widths required an automated procedure as the reliability in cursor selected diameters initially proved insufficient to capture the necessary detail. A semi-automated procedure was developed and Fig. 5.4 documents graphically the steps of the process. Raw image files taken by SEM are thresholded in ImageJ by the automatic threshold. Using the automated thresholding procedure eliminates a layer of judgement regarding where the inside of the hole begins and where the ragged edge of the exposure ends. The image is inverted by ImageJ software to yield a black and white image. MS Paint is then used to flood the image to distinguish the resistless regions within the holes from the edges and background. The inner radius of the relief is the diameter sought as this is the extent of the domain where substrate etching will occur. Some measurements are lost by this flooding if the hole edge is particularly ragged (Fig. 5.3 c)). The particle analysis routine in ImageJ calculates these islands' area and their distribution. These particle areas are plotted in Fig. 5.3 d) showing that it is typically very straightforward to distinguish the real particles from the noise. These particle areas are converted to hole diameters in pixels and then scaled ap-

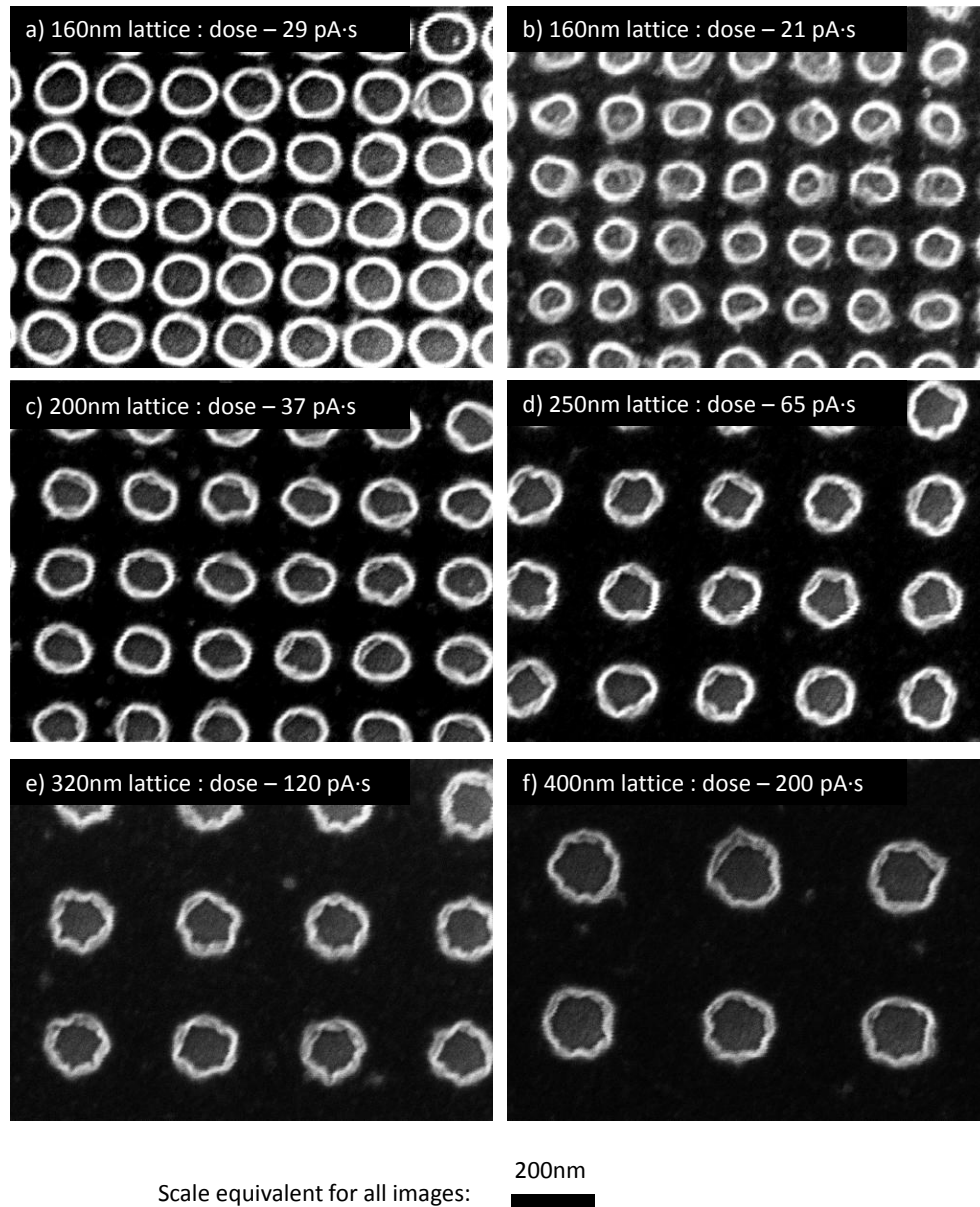


**Figure 5.3:** Comparison of images a) and b) demonstrates hole-size modification by altering the dose at one lattice size. Comparison of images b) through f) demonstrates the requirement of increasing dose strength to maintain an approximately constant hole-width to lattice-spacing ratio. All doses are reported as electrical charge delivered per spot.

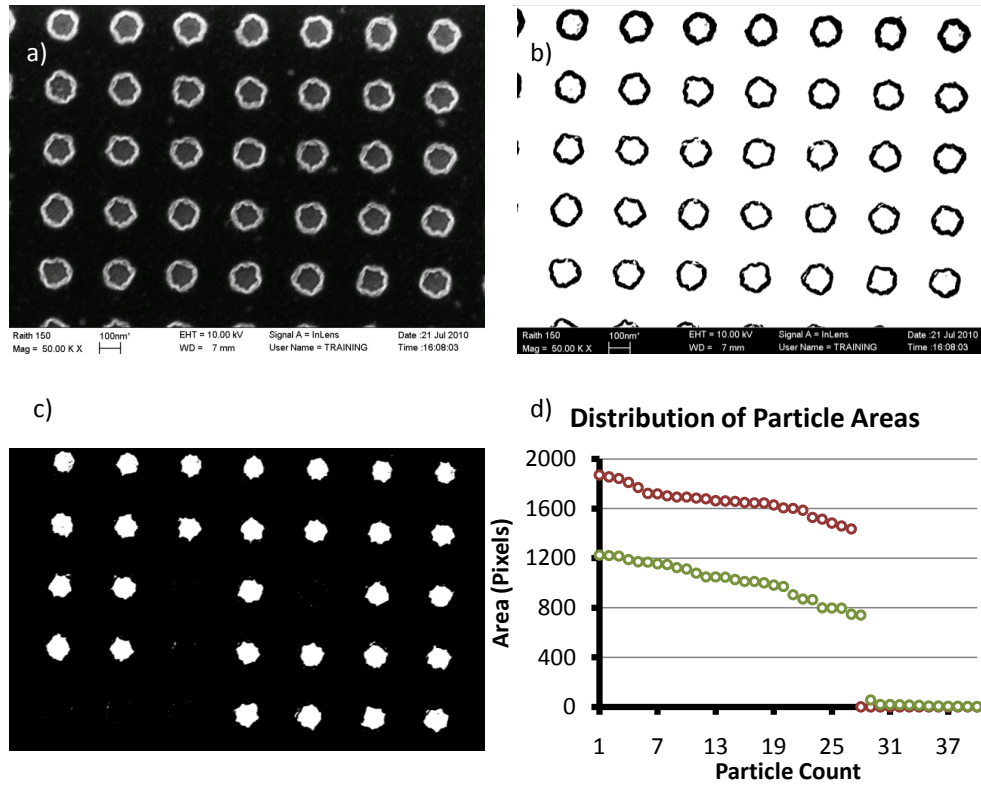


**Figure 5.4:** The raw image file taken by SEM a) has an automatic threshold applied by ImageJ software and is inverted to yield a black and white image b) of the relief seen at the edges of the holes. This image is flooded using MS Paint to yield islands c) representative of the uncovered quartz. An ImageJ particle analysis routine calculates the area of each island yielding a distribution of particle areas d) from which the noise is easily eliminated and an average hole width is calculated. The red curve represents the area distribution calculated from this image; the green from another.

appropriately to yield an average and standard deviation in hole width.

The hole width data recorded for a range of doses and a range of lattice spacings are plotted as ellipsoids in 3D space in Fig. 5.5. The ellipsoids' radius along the three axes is representative of the standard deviation in measuring these parameters. A surface is then fit to this data to allow prediction of the dose requirements for creating holes of arbitrary width and

Hole Clearance Width as a Function of Electron Beam Dose and Lattice Spacing

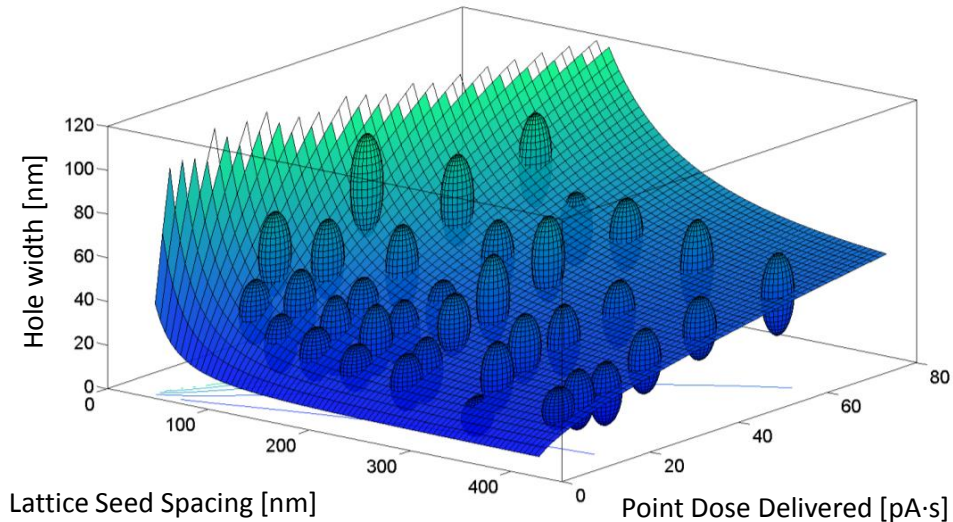


**Figure 5.5:** Results of preliminary investigation of lattice-dose combinations and the resulting resist hold width. Ellipsoid radii are representative of uncertainty in measurement. Fit surface described by Eq. 5.1 with parameters given in Eq. 5.2.

lattice spacing. The function formulation describing this surface is based on previously established qualitative descriptions of how the electron exposure occurs in the film.

It is known that there will be some contribution to the exposure of the resist by the widely backscattered electrons typically responsible for the proximity effect in aperiodic electron beam lithography exposures. When averaged over the large patterned area this widely backscattered dose should be proportional to incident charge areal density. It is accounted for by the first term in Eq. 5.1 where  $C_1$  is used to permit nonlinearity and  $C_2$  represents the characteristic length of the backscatter area. The second term accounts

for the exposure contribution from direct electron beam exposure, and  $C_3$  relates the clearing strength of forward scattering electrons with  $C_4$  once again permitting a nonlinearity in the response.

$$HoleWidth = PointDose^{C_1} \times \left( \frac{C_2}{LatticeSize} \right)^2 + C_3 \times PointDose^{C_4} \quad (5.1)$$

$$\begin{aligned} C_1 &= 0.8776 \\ \text{Constants to fit surface in Eq. 5.1} \quad C_2 &= 186.9 \\ \text{to preliminary dataset} \quad C_3 &= 5.806 \\ C_4 &= 0.4260 \end{aligned} \quad (5.2)$$

The surface is fit using least squares yielding the resulting constants displayed in Eq. 5.2. The data samples initially chosen did not span the entire necessary domain of interest in lattice spacing and dose requirements. Thus, this surface was extrapolated to hypothesize appropriate dose-lattice combinations for further experiments.

The resulting hole-width relationships from the subsequent investigation are shown in Fig. 5.6 The surface is fit using least squares yielding the resulting constants displayed in Eq. 5.3. The changes to these constants are within reason as the domain spans a significantly larger dose-lattice combination domain. The ideal curve representing a recipe that should yield hole

Hole Clearance Width as a Function of Electron Beam Dose and Lattice Spacing

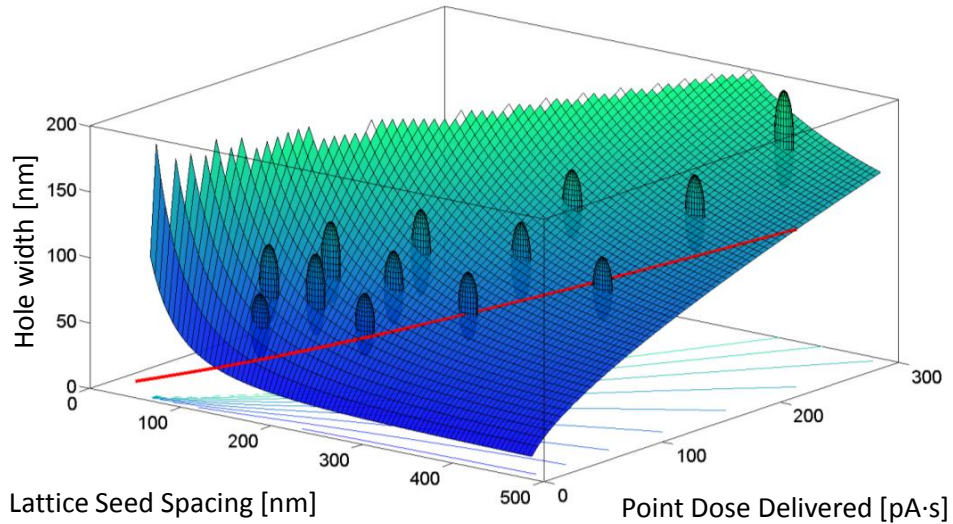


**Figure 5.6:** Results of the second investigation of lattice-dose combinations and the resulting resist hole width. Data domain of lattice spacing and point dose combinations is the result of predicted combinations from the surface calculated in Fig. 5.5. Ellipsoid radii are representative of uncertainty in measurement. Fit surface described by Eq. 5.1 with parameters given in Eq. 5.3. Red line indicates position of lattice-dose combination to yield hole widths of 25% of lattice spacing.

widths of exactly 25% is shown as a red line.

$$\begin{aligned}
 C_1 &= 0.8826 \\
 \text{Constants to fit surface in Eq. 5.1} \quad C_2 &= 286.0 \\
 \text{to secondary dataset} \quad C_3 &= 6.436 \\
 C_4 &= 0.4571
 \end{aligned}
 \tag{5.3}$$

### 5.2.3 Quartz stamp processing

One eighth inch thick pieces of quartz were diced into 20 mm squares, washed and then cleaned of organic residues in a hot 3:1  $\text{H}_2\text{SO}_4:\text{H}_2\text{O}_2$  piranha bath for 15 minutes. Adsorbed water was driven from the surface by baking at  $200^\circ\text{C}$  for 5 minutes. PMMA 950k was spread on these squares using an automated spinning process ramping to 1000 rpm at 250 rpm/sec and thinning the resist for 10 seconds. The spin process was then ramped by 1000 rpm/sec and the resist was thinned at 4000 rpm for 30 seconds before slowing to a stop at 500 rpm/sec. Subsequently baking them at  $180^\circ\text{C}$  for 10 minutes drove the solvent out of the resist. An  $\sim 8$  nm aluminum anti-charging layer was sputtered on using a standard process for 35 seconds at a deposition rate of nominally 13.4 nm/min. Patterns were exposed using the Raith 150 electron beam lithography system following all the standard protocols for focus and alignment. Write-field sizes of 100 microns were employed. Beam parameters were set at 10 kV accelerating voltage and a  $20\ \mu\text{m}$  aperture. These settings typically yielded an approximately 80 nA current with an estimated variation of 0.5% ( $1\sigma$ ). The aluminum layer was removed by soaking the now-patterned quartz in MF-CD26 for 120 seconds and subsequently rinsing in water and blowing dry using nitrogen. The PMMA was then developed in a 1:3 methyl isobutyl ketone : isopropyl alcohol (MIBK:IPA) developer solution. Thirty seconds development using con-

stant but gentle manual agitation was performed. Following the MIBK:IPA development the sample was immediately moved into a pure IPA stopper bath for a further 30 seconds. Following this, the quartz stamp was immediately plunged into water and rinsed thoroughly before being blown dry again using nitrogen.

Pattern transfer from the PMMA resist into the quartz stamp was done using a standard silicon dioxide etching procedure for a period of 25 seconds using a Surface Technology Systems two wafer load locked reactive ion etch system. Three process gasses were flowed into the etching chamber ( $O_2$ : 5 sccm,  $CF_4$ : 20 sccm and  $CHF_3$ : 30 sccm) and the vacuum throttle was controlled to maintain a pressure of 100 mTorr. An etching power of 300 W was maintained through computer controlled feedback requiring  $900 \pm 80 V_{DC}$ . The residual PMMA was removed by soaking the stamp in acetone for 30 minutes, rinsing thoroughly and then removing all other organic residue using a cold 3:1  $H_2SO_4:H_2O_2$  piranha bath for 15 minutes. At this point, the stamp surface may be functionalized to limit nanoimprint resist adhesion to it during processing. For further functionalization the stamps were placed in a vacuum desiccator alongside a small vial containing a few drops of perchlorosilane for a period of 3 to 6 hours. This period of time was sufficient for a monolayer of the perchlorosilane to interact with the glass surface and render it highly hydrophobic. At this point the stamp was ready to be used for imprinting.

### 5.3 Imprint lithography of seeds

A commercial Nanonex universal imprinter system is used to imprint seeds from these stamps. These steps are diagrammed in Fig. 5.2 d)-e). The proprietary thermoplastic NanoImprint lithography resist, NXR-1025 2.5% solution, was used. This resist is spread at 2500 rpm for 60 seconds onto piranha cleaned silicon <100> 20mm squares. Following spinning the resist, the residual solvent was driven off by baking on a hotplate at 150°C for 240 seconds. The standard process for imprinting using the NXR-1025 resist was followed. Pressure at 200 psi was established on the air-cushion press within the system and the temperature was cycled to 120°C while monitored by thermocouple for 30 seconds duration. Following releasing of the pressure, the sample was pried off of the stamp with a razor blade.

A final etching step to transfer the resist topography from the thermally imprinted resist to the silicon substrate (Fig. 5.2f) was tested using a reactive ion etch with preferential silicon selectivity but was ultimately unnecessary. Instead, the relief present in Fig. 5.2e was determined to be acceptable to serve as a seeding layer for GLAD. Some applications will not permit the presence of an organic layer like this, but for strictly seeding a film to be optically characterized it would have no effect. Situations requiring electrical conductivity between GLAD posts and the substrate, for example, would require further process development to establish a working etch process to

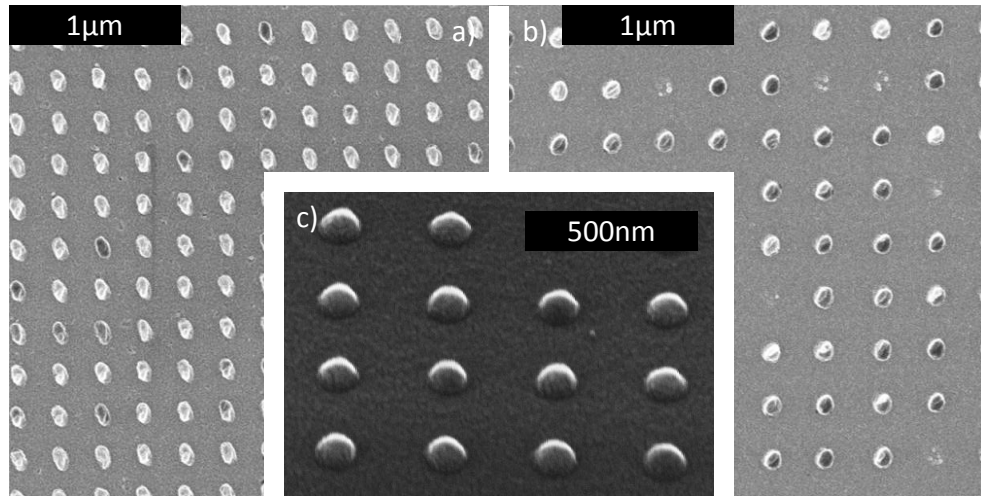


**Figure 5.7:** Seeds fabricated by NanoImprint Lithography. Top down images taken using a scanning electron microscope of seeds patterned in an a) 250 nm and b) 320 nm lattice. Image c) shows an oblique view of seeds patterned on a 400 nm lattice.

transfer seed topography into the substrate.

The seeds produced are displayed in Fig. 5.7. Their cross section appears based on observation by SEM to be roughly hemispherical and between 50 nm and 80 nm in height. The seeds formed on the 320 nm lattice have diameters equal to approximately 38% of the lattice spacing, very amenable to use for fabrication of square spiral photonic crystals.

A single large area array stamp with a circular patterned area 5 mm in diameter was fabricated based on a 320 nm lattice spacing. Stamps with lattice spacings of 80 nm, 100 nm, 125 nm, 160 nm, 200 nm, 250 nm, 320 nm, and 400 nm were also fabricated in square 1 mm areas. These stamp spacings span the range of useful seeding patterns for use with GLAD for most typical materials. Overly aggressive seeding patterns, either too closely packed

or too sparsely packed will fail to exhibit favourable growth mechanics, and the control that is typically gained by seeding is instead lost.

## 5.4 Deposition of square spiral photonic crystals by

### GLAD

GLAD films were deposited onto seeded substrates with patterned lattice spacings of 320 nm. A 6.5 kV accelerating voltage and a 300 mA electrical current are used to evaporate  $\text{TiO}_2$  in an electron beam evaporator. The depositions began with chamber pressures less than  $10^{-5}$  Torr which fell to near  $2 \times 10^{-5}$  Torr by the end of the deposition. A crystal thickness monitor used during the deposition measured the deposition rate to vary between 0.4 and 0.6 nm/s. A substrate motion control algorithm is used in conjunction with this thickness monitor to employ a PhiSweep technique, with 8 sweeps per square spiral arm. A  $26.5^\circ$  PhiSweep angle was selected as this has been shown to be optimal [54]. The PhiSweeps are ordered such that between arms, the transition is from inward-pointing to outward-pointing. This maximizes the column height gain between spiral arms, performing a similar function to the slow corner technique [52]. A deposition angle of  $\alpha = 86^\circ$  is used and control over  $\phi$  was calculated based on a 320 nm lattice design. The films were grown to a design thickness of 2176 nm based on a five turn square spiral architecture.

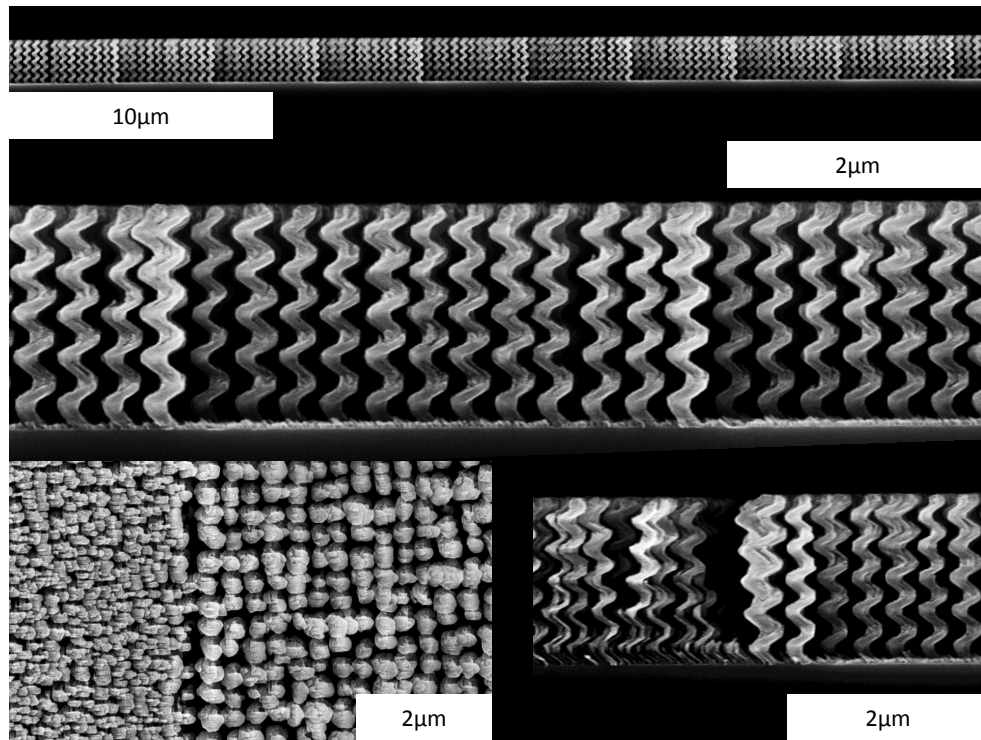


**Figure 5.8:** Three different side-shots of a  $\text{TiO}_2$  photonic crystal deposited on a 320 nm lattice at  $\alpha = 86^\circ$ . The crystal structure is highly repeatable over a very large area ( $20 \text{ mm}^2$ ). At bottom a top view and side view of two (different) photonic crystals at the juncture between seeded and unseeded areas of the substrate.

### 5.4.1 Optical characterization

Images depicting one film are in Fig. 5.8. Excellent uniformity is seen in this film throughout the  $\sim 2 \mu\text{m}$  thickness and across the large area seeding pattern. The square spiral's geometrical properties offer a more straightforward method of determining the structured thin film's degree of optimization than the optical characteristics. The parameters characterizing the optimal geometry are commonly listed as three scalar values  $[L, c, r]$  after [36] (see Fig. 2.5). These are measurements of spiral size in units of lattice spacing.  $L$  indicates the horizontal length of a single spiral arm,  $c$ , one unit cell's height, and  $r$ , the spiral arm's circular cross section radius. The geometric parameters of the best photonic crystal structure fabricated remain rather unoptimized and were measured as  $[L, c, r] = [0.46, 1.05, 0.15]$  compared to the optimal diamond:1 geometry described as  $[L, c, r] = [0.70, 1.35, 0.20]$  [55]. This does not constitute square spiral geometry specific enough to the diamond lattice to form a complete bandgap where tolerances generally must be within 10% of the optimal values. However, for an initial attempt this is promising, and the changes necessary to achieve a complete photonic bandgap likely have workable solutions.

The optical properties when observed with the naked eye indicate that the film is optically active in the seeded region, the observed color of the film distinctly changes with azimuth and inclination and reflectance peaks

are observed for some incident angles. The film's normal reflectance was measured and the results are shown in Fig. 5.9 where a likely photonic bandgap is observed to exist in the region of 440 nm. This bandgap exists in clear contrast to the unseeded region of the same film. The interference fringes seen between 500 nm and 700 nm of Fig. 5.9 arise from the finite size of the crystal for both the seeded and unseeded cases.

The geometric parameters of this film suggest that the optical path length of the periodicity of the film in the normal direction should be close to 475 nm nearly matching the location of the bandgap center at 440 nm. Toader predicts [55] the location of the bandgap center for an optimized silicon square spiral photonic crystal to arise at 880 nm when deposited on seeds with a 320 nm periodicity. Considering that the wavelength of light in silicon is 40% shorter than in anatase TiO<sub>2</sub> a rough approximation to the theoretical location of an optimized bandgap center wavelength would be 637 nm. When corrected for the unoptimized nature of this crystal's unit cell in the vertical dimension this would predict a bandgap at 495 nm. Both estimations predict the wavelength domain of interest reasonably well.

## 5.5 Summary

A method to fabricate an imprinting stamp for use with a nanoimprint lithography system is described based on electron beam lithography. For

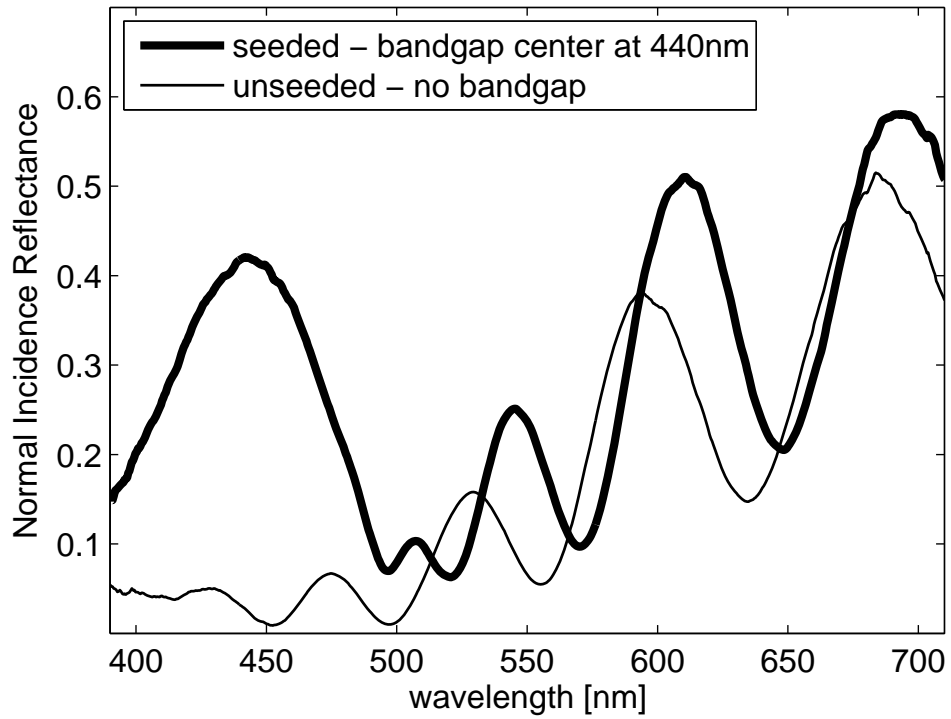


**Figure 5.9:** A distinct difference in the spectrum is observed between the stochastically ordered spirals and the seeded area of the substrate where the square spirals are spaced to create a regular periodicity in all three dimensions. A bandgap appears to be centered at approximately 440 nm wavelength in the seeded photonic crystal and none is observed in the unseeded film.

a wide range of desired seed-spacing requirements electron beam lithography point exposure doses are defined for patterning PMMA to result in accurate hole widths of 25% of the lattice spacing. Nanoimprint lithography stamps are prepared using this technique to create seeding arrays to fabricate square spiral photonic crystals. GLAD films of  $\text{TiO}_2$  are deposited onto these seeds using an unoptimized square spiral deposition algorithm. The resulting photonic crystal thin film whose growth has been assisted by the seeds exhibits bandgap properties whereas the unseeded film does not. Deposition optimization is likely to yield a complete photonic bandgap.

## CHAPTER 6

# CONCLUSIONS AND DIRECTIONS FOR FUTURE WORK

### 6.1 Research summary

Chapter 3 demonstrated that a photonic crystal's reflectance spectrum may be controlled by dye molecule electrophoretic motion within a switching device. The absorption of the dye infiltrating the porous photonic crystal altered the device's optical state, yet this state could be partly reversed by an electric field. A custom reflectance measurement apparatus was designed and optimized to record these devices' optical properties. This chapter also explored a wide range of factors impairing device performance and their correction was observed to improve reliability and quality in a second generation of devices. Dye motion in these devices resulted in controlled and

repeatable reflectance changes up to 0.4 in absolute reflectance.

In Chapter 4, the response time of the cells was investigated as an avenue to explore the optical phenomenon that give rise to the reflectance changes quantified in Chapter 3. By fitting exponential curves to the response time-series optical data it was possible to quantify how quickly the optical properties could be changed by electrically addressing the cell and causing dye molecule motion. The GLAD film's porous nature contributed to the hysteresis observed in response time between dye inflow and dye outflow from the photonic crystal. The photonic crystal's photonic bandgap gave rise to a wavelength dependence in the response curves, an explanation was proposed arising from a group velocity mismatch between band-edge and bandgap-center wavelengths. Modelling this phenomenon confirmed that it would give rise to the observed effects and that the approximate magnitude in variation between band-edge and bandgap-center wavelengths was in line with the experimental results.

Electron beam lithography was used in Chapter 5 to create an imprinting mask for use with nanoimprint lithography. This imprinting stamp was used to create seeding arrays which were capable of nucleating GLAD thin film growth. This seeding phenomenon was used to fabricate a square spiral 3D photonic crystal of  $\text{TiO}_2$ . The still unoptimized geometry exhibited a distinct bandgap near 440 nm, in film regions where the growth was seeded, and no bandgap when seeding does not occur.

## 6.2 Short term future research suggestions

In Chapter 3, Fig. 3.6 showed a distinct bias for the direction in which the spectrum may be modified by applying an electric field. Across the three voltages explored in this image, the positive polarity results in rather significant changes with addressing voltage while the negative polarity does not show such distinct voltage dependence. We might hypothesize that this has not been observed previously due to the concentrated dye solution used. Operating at very high dye concentrations, while seeming to provide strong response results, may have prevented achieving the largest switching ranges possible. If the dye's solubility limit was interacting with its electrophoretic motion, this effect was undetectable by the methods employed here. It may be possible for the dye's relative absorption to be increased by electrophoretically driving cations into the photonic crystal with the application of a negative voltage to the front electrode. Such a situation might result in response curves that are equally sensitive to positive and negative addressing voltage polarities. Further work with dilute methylene blue molecule solutions would need to be pursued to address this question.

Chapters 3 and 4 fail to fully address the potential for optimizing the methylene blue cell's response in terms of potential application. A photonic crystal display application would require a large reflectance change as well as a faster response time than those observed throughout Chapter 4. Fab-

ricating cells with reservoir gaps at less than  $55 \mu\text{m}$  would help to address the issue of electric field strength. It is also possible to address the cell using a voltage signal that differs from a square wave. The square wave was used in this work for its simplicity, there is no reason to believe that its effect on the dye molecules motion results in anything close to an optimal response pattern. With further optimization, video-rate switching is likely possible.

Work done in Chapter 5 was left highly unoptimized. The square spiral photonic crystal co-ordinates:  $[L, c, r] = [0.46, 1.05, 0.15]$  could almost certainly be improved upon. Coordinates  $L$  and  $c$ , representing the spiral width and pitch height respectively, are coupled when using the GLAD technique and it is initially only a matter of scaling the deposition by approximately 40% to achieve a photonic crystal structure that has an  $L$  parameter within 8% of optimum and a  $c$  parameter within 9% of optimum. These results may be brought even closer to ideal by further refining some deposition parameters; the deposition angle  $\alpha$ , and the number of phi-sweeps per arm. Post-width, related to the third co-ordinate  $c$ , may be adjusted by annealing or atomic layer deposition and is the only parameter that may be modified post-deposition. In this regard, so long as  $c$  is smaller than ideal it may be presumed that this could be perfectly idealized. Noting the predicted parameters for  $L$  and  $c$  before any further optimization of  $\alpha$  during deposition it can reasonably be expected that a photonic crystal with a complete photonic bandgap of at least 3.1% is possible using anatase  $\text{TiO}_2$ .

### 6.3 Avenues for future long term research

The work presented on dye electrophoresis investigated only methylene blue in a  $\text{TiO}_2$  photonic crystal. This combination proved to be successful as a first attempt but it was by no means optimized for any performance metrics. Stronger absorbing dyes exist, and the use of dye combinations are certainly possible to locate the switching response arbitrarily anywhere along the wavelength spectrum. One potentially interesting phenomenon that may be investigated is using a dye such as methylene blue which has an absorbing cation with a large acid residue molecule with absorptive properties. Such a combination within an electrophoretic cell would result in an addressing voltage in one polarity moving a dye affecting one wavelength domain into the photonic crystal and simultaneously driving out the dye affecting another wavelength domain. A photonic crystal may be designed to exhibit a bandgap spanning the wavelength domain between the two dyes' peak absorbances. In Chapter 3 we observed a 16nm band-edge shift due to dye motion. Replicating this result at both the upper and lower band edges operating in opposite directions to one another would result in a bandgap shifting cell capable of approximately a 16 nm center wavelength shift.

While chapter 5 identified the fact that electrophoretic switching would not be possible while maintaining a complete 3D photonic bandgap within a  $\text{TiO}_2$  square spiral crystal, this achievement should not be considered im-

possible. Admittedly the challenge is daunting, but infiltrating the photonic crystal with a medium with a controllable refractive index is a potential method. One such method would be infiltration with a critical-point fluid. By modulating the temperature and/or the pressure of the system at the fluid's critical point it may be possible to switch the photonic bandgap. This applicability of this method to realistic applications is minimal. The very high temperatures and pressures required would require much more specialized apparatus than the cell design employed for the investigation of electrophoretic based switching. It may however provide significant scientific insight into photonic bandgap behaviour. In this regard, pursuing this is more than an end unto itself.

## REFERENCES

- [1] K. Yoshino, Y. Kawagishi, M. Ozaki, and A. Kose, "Mechanical Tuning of the Optical Properties of Plastic Opal as a Photonic Crystal," *Japanese Journal of Applied Physics*, vol. 38, pp. L786–L788, July 1999.
- [2] H. Fudouzi and Y. Xia, "Colloidal Crystals with Tunable Colors and Their Use as Photonic Papers," *Langmuir*, vol. 19, pp. 9653–9660, Nov. 2003.
- [3] J. Li, W. Huang, and Y. Han, "Tunable photonic crystals by mixed liquids," *Colloids and Surfaces A: Physicochemical and Engineering Aspects*, vol. 279, pp. 213–217, May 2006.
- [4] C.-T. Chan and J. A. Yeh, "Tunable photonic crystal based on capillary attraction and repulsion," *Optics Express*, vol. 18, p. 20894, Sept. 2010.
- [5] Y. Huang, Y. Zhou, C. Doyle, and S.-T. Wu, "Tuning the photonic band gap in cholesteric liquid crystals by temperature-dependent dopant solubility," *Optics Express*, vol. 14, p. 1236, Feb. 2006.
- [6] Y. Shimoda, M. Ozaki, and K. Yoshino, "Electric field tuning of a stop band in a reflection spectrum of synthetic opal infiltrated with nematic liquid crystal," *Applied Physics Letters*, vol. 79, no. 22, p. 3627, 2001.
- [7] F. Guinneton, "Optimized infrared switching properties in thermochromic vanadium dioxide thin films: role of deposition process and microstructure," *Thin Solid Films*, vol. 446, pp. 287–295, Jan. 2004.
- [8] M. Soltani, M. Chaker, E. Haddad, R. V. Kruzelecky, and D. Nikanpour, "Optical switching of vanadium dioxide thin films deposited by reactive pulsed laser deposition," *Journal of Vacuum Science & Technology A: Vacuum, Surfaces, and Films*, vol. 22, p. 859, May 2004.
- [9] X. Xu, G. Friedman, K. D. Humfeld, S. A. Majetich, and S. A. Asher, "Synthesis and Utilization of Monodisperse Superparamagnetic Colloidal Particles for Magnetically Controllable Photonic Crystals," *Chemistry of Materials*, vol. 14, pp. 1249–1256, Mar. 2002.

## REFERENCES

---

- [10] K. Busch and S. John, "Liquid-Crystal Photonic-Band-Gap Materials: The Tunable Electromagnetic Vacuum," *Physical Review Letters*, vol. 83, pp. 967–970, Aug. 1999.
- [11] M. Ozaki, Y. Shimoda, M. Kasano, and K. Yoshino, "Electric field tuning of the stop band in a liquid-crystal-infiltrated polymer inverse opal," *Adv. Mater.*, vol. 14, p. 514, 2002.
- [12] J. D. Joannopoulos, P. R. Villeneuve, and S. Fan, "Photonic crystals: putting a new twist on light," *Nature*, vol. 386, pp. 143–149, Mar. 1997.
- [13] M. Born and E. Wolf, "Principles of Optics Electromagnetic Theory of Propagation, Interference and Diffraction of Light 2nd edition," *Principles of Optics Electromagnetic Theory of Propagation, Interference and Diffraction of Light 2nd edition by Max Born, Emil Wolf New York, NY: Pergamon Press, 1964*, vol. -1, 1964.
- [14] P. S. J. Russell, S. Tredwell, and P. J. Roberts, "Full photonic bandgaps and spontaneous emission control in 1D multilayer dielectric structures," *Optics Communications*, vol. 160, no. 1-3, pp. 66–71, 1999.
- [15] E. Yablonovitch, "Inhibited Spontaneous Emission in Solid-State Physics and Electronics," *Physical Review Letters*, vol. 58, pp. 2059–2062, May 1987.
- [16] S. John, "Strong localization of photons in certain disordered dielectric superlattices," *Physical Review Letters*, vol. 58, pp. 2486–2489, June 1987.
- [17] J. Drake and A. Genack, "Observation of nonclassical optical diffusion," *Physical Review Letters*, vol. 63, pp. 259–262, July 1989.
- [18] K. Ho, C. Chan, and C. Soukoulis, "Existence of a photonic gap in periodic dielectric structures," *Physical Review Letters*, vol. 65, pp. 3152–3155, Dec. 1990.
- [19] S. Satpathy, Z. Zhang, and M. R. Salehpour, "Theory of photon bands in three-dimensional periodic dielectric structures," *Phys. Rev. Lett.*, vol. 64, pp. 1239–1242, Mar. 1990.
- [20] E. Yablonovitch and T. J. Gmitter, "Photonic band structure: The face-centered-cubic case," *Phys. Rev. Lett.*, vol. 63, pp. 1950–1953, Oct. 1989.
- [21] Y. Xia, B. Gates, and Z.-Y. Li, "Self-Assembly Approaches to Three-Dimensional Photonic Crystals," *Advanced Materials*, vol. 13, pp. 409–413, Mar. 2001.

- [22] M. Maldovan, C. K. Ullal, W. C. Carter, and E. L. Thomas, "Exploring for 3D photonic bandgap structures in the 11 f.c.c. space groups," *Nat Mater*, vol. 2, pp. 664–667, Oct. 2003.
- [23] J. Joannopoulos, "Photonic crystals," *Solid State Communications*, vol. 102, pp. 165–173, Apr. 1997.
- [24] J. D. Joannopoulos, "Minding the gap," *Nature*, vol. 375, pp. 278–278, May 1995.
- [25] E. Yablonovitch, T. Gmitter, R. Meade, A. Rappe, K. Brommer, and J. Joannopoulos, "Donor and acceptor modes in photonic band structure," *Physical Review Letters*, vol. 67, pp. 3380–3383, Dec. 1991.
- [26] K. Ho, C. Chan, C. Soukoulis, R. Biswas, and M. Sigalas, "Photonic band gaps in three dimensions: New layer-by-layer periodic structures," *Solid State Communications*, vol. 89, pp. 413–416, Feb. 1994.
- [27] S. Y. Lin, J. G. Fleming, D. L. Hetherington, B. K. Smith, R. Biswas, K. M. Ho, M. M. Sigalas, W. Zubrzycki, S. R. Kurtz, and J. Bur, "A three-dimensional photonic crystal operating at infrared wavelengths," *Letters to Nature*, vol. 394, pp. 251–253, July 1998.
- [28] S. Noda, N. Yamamoto, H. Kobayashi, M. Okano, and K. Tomoda, "Optical properties of three-dimensional photonic crystals based on II-V semiconductors at infrared to near-infrared wavelengths," *Applied Physics Letters*, vol. 75, no. 7, p. 905, 1999.
- [29] T. Katsuyama, K. Hosomi, H. Yamada, S. Goto, K. Aoki, and Y. Arakawa, "Woodpile photonic crystals composed of air columns," *Photonics and Nanostructures - Fundamentals and Applications*, vol. 4, pp. 54–58, Feb. 2006.
- [30] Z. Ming, K. Jun-Jie, Y. Hai-Feng, Y. Feng, and C. Lan, "Rapid Fabrication of Three-Dimensional Woodpile Photonic Crystals by Means of Two-Photon Photopolymerization," *Chinese Physics Letters*, vol. 24, pp. 3164–3167, Nov. 2007.
- [31] A. van Blaaderen, R. Ruel, and P. Wiltzius, "Template-directed colloidal crystallization," *Nature*, vol. 385, pp. 321–324, Jan. 1997.
- [32] A. Blanco, E. Chomski, S. Grabtchak, M. Ibisate, S. John, S. Leonard, C. Lopez, F. Meseguer, H. Miguez, J. Mondia, G. Ozin, O. Toader, and van Driel HM, "Large-scale synthesis of a silicon photonic crystal with a complete three-dimensional bandgap near 1.5 micrometres," *Nature*, vol. 405, pp. 437–40, May 2000.

- [33] Y. A. Vlasov, X. Z. Bo, J. C. Sturm, and D. J. Norris, "On-chip natural assembly of silicon photonic bandgap crystals," *Nature*, vol. 414, pp. 289–93, Nov. 2001.
- [34] E. Palacios-Lidon, A. Blanco, M. Ibasate, F. Meseguer, C. LoApez, and J. SaAanchez-Dehesa, "Optical study of the full photonic band gap in silicon inverse opals," *Applied Physics Letters*, vol. 81, p. 4925, Dec. 2002.
- [35] D. P. Aryal, K. L. Tsakmakidis, C. Jamois, and O. Hess, "Complete and robust bandgap switching in double-inverse-opal photonic crystals," *Applied Physics Letters*, vol. 92, p. 011109, Jan. 2008.
- [36] O. Toader and S. John, "Proposed square spiral microfabrication architecture for large three-dimensional photonic band gap crystals," *Science (New York, N.Y.)*, vol. 292, pp. 1133–5, May 2001.
- [37] J. H. Moon, S. Yang, W. Dong, J. W. Perry, A. Adibi, and S.-M. Yang, "Core-shell diamond-like silicon photonic crystals from 3D polymer templates created by holographic lithography," *Optics Express*, vol. 14, p. 6297, June 2006.
- [38] G. Liang, X. Zhu, Y. Xu, J. Li, and S. Yang, "Holographic design and fabrication of diamond symmetry photonic crystals via dual-beam quadruple exposure," *Advanced materials (Deerfield Beach, Fla.)*, vol. 22, pp. 4524–9, Oct. 2010.
- [39] M. Maldovan and E. L. Thomas, "Diamond-structured photonic crystals," *Nature materials*, vol. 3, pp. 593–600, Sept. 2004.
- [40] K. Robbie, "Sculptured thin films and glancing angle deposition: Growth mechanics and applications," *Journal of Vacuum Science & Technology A: Vacuum, Surfaces, and Films*, vol. 15, p. 1460, May 1997.
- [41] K. Robbie, M. J. Brett, and A. Lakhtakia, "Chiral sculptured thin films," *Nature*, vol. 384, no. 6610, p. 616, 1996.
- [42] K. Robbie, "Advanced techniques for glancing angle deposition," *Journal of Vacuum Science & Technology B: Microelectronics and Nanometer Structures*, vol. 16, p. 1115, May 1998.
- [43] D. Gish, M. Summers, and M. Brett, "Morphology of periodic nanostructures for photonic crystals grown by glancing angle deposition," *Photonics and Nanostructures - Fundamentals and Applications*, vol. 4, pp. 23–29, Feb. 2006.

- [44] M. O. Jensen and M. J. Brett, "Porosity engineering in glancing angle deposition thin films," *Appl. Phys. A.*, vol. 80, no. 4, pp. 763–768, 2005.
- [45] J. C. Sit, D. Vick, K. Robbie, and M. J. Brett, "Thin film microstructure control using glancing angle deposition by sputtering," *Optics Lett.*, vol. 29, no. 21, pp. 2545–2547, 2004.
- [46] Y. W. Sun, J. Gospodyn, P. Kurska, J. Sit, R. G. DeCorby, and Y. Y. Tsui, "Dense and porous ZnO thin films produced by pulsed laser deposition," *Applied Surface Science*, vol. 248, no. 1-4, pp. 392–396, 2005.
- [47] J. J. Steele, M. T. Taschuk, and M. J. Brett, "Nanostructured metal oxide thin films for humidity sensors," *IEEE Sensors J*, vol. 8, no. 7-8, pp. 1422–1429, 2008.
- [48] A. C. van Popta, M. M. Hawkeye, J. C. Sit, and M. J. Brett, "Gradient-index narrow-bandpass filter fabricated with glancing-angle deposition," *Optics Letters*, vol. 29, p. 2545, Nov. 2004.
- [49] A. Chutinan and S. Noda, "Spiral three-dimensional photonic-bandgap structure," *Physical Review B*, vol. 57, pp. R2006–R2008, Jan. 1998.
- [50] S. R. Kennedy, M. J. Brett, O. Toader, and S. John, "Fabrication of Tetragonal Square Spiral Photonic Crystals," *Nano Lett.*, vol. 2, no. 1, pp. 59–62, 2002.
- [51] S. Kennedy, "Optical properties of a three-dimensional silicon square spiral photonic crystal," *Photonics and Nanostructures - Fundamentals and Applications*, vol. 1, pp. 37–42, Dec. 2003.
- [52] S. R. Kennedy and M. J. Brett, "Advanced techniques for the fabrication of square spiral photonic crystals by glancing angle deposition," *Journal of Vacuum Science & Technology B: Microelectronics and Nanometer Structures*, vol. 22, p. 1184, May 2004.
- [53] M. Summers, *Periodic thin films by glancing angle deposition*. Phd, University of Alberta, Edmonton, AB, Canada, 2009.
- [54] M. A. Summers and M. J. Brett, "Optimization of periodic column growth in glancing angle deposition for photonic crystal fabrication," *Nanotechnology*, vol. 19, p. 415203, Oct. 2008.
- [55] O. Toader and S. John, "Square spiral photonic crystals: Robust architecture for microfabrication of materials with large three-dimensional photonic band gaps," *Physical Review E*, vol. 66, p. 016610, July 2002.
- [56] F. Duarte, L. Hillman, and (Eds.), *Dye laser principles, with applications*. New York: Academic Press, Jan. 1990.

- [57] G. N. Lewis, O. Goldschmid, T. T. Magel, and J. Bigeleisen, "Dimeric and Other Forms of Methylene Blue: Absorption and Fluorescence of the Pure Monomer1," *Journal of the American Chemical Society*, vol. 65, no. 6, pp. 1150–1154, 1943.
- [58] S. Murai, K. Fujita, K. Nakanishi, and K. Hirao, "Fabrication of dye-infiltrated macroporous silica for laser amplification," *Journal of Non-Crystalline Solids*, vol. 345-346, pp. 438–442, Oct. 2004.
- [59] S. Machida, T. Sugihara, S. Masuo, and A. Itaya, "Photoluminescence properties of dye-doped polymer multilayer films with periodic structure," *Thin Solid Films*, vol. 516, no. 9, pp. 2382–2386, 2008.
- [60] M. M. Lezhnina and U. H. Kynast, "Inverse opals hosting rare earth species," *Journal of Alloys and Compounds*, vol. 451, no. 1-2, pp. 545–548, 2008.
- [61] M. Alencar, G. Maciel, C. Dearaujo, R. Bertholdo, Y. Messaddeq, and S. Ribiero, "Laserlike emission from silica inverse opals infiltrated with Rhodamine 6G," *Journal of Non-Crystalline Solids*, vol. 351, pp. 1846–1849, July 2005.
- [62] J. T. Remillard, J. M. Ginder, and W. H. Weber, "Evanescent-wave scattering by electrophoretic microparticles: a mechanism for optical switching," *Applied Optics*, vol. 34, p. 3777, July 1995.
- [63] M. A. Mossman, V. H. Kwong, and L. A. Whitehead, "A novel reflective image display using total internal reflection," *Displays*, vol. 25, no. 5, pp. 215–221, 2004.
- [64] P. MušLrau and B. Singer, "The understanding and elimination of some suspension instabilities in an electrophoretic display," *Journal of Applied Physics*, vol. 49, no. 9, p. 4820, 1978.
- [65] P. C. P. Hruđey, M. A. Martinuk, M. A. Mossman, A. C. van Popta, M. J. Brett, T. D. Dunbar, J. S. Huizinga, and L.A. Whitehead, "Application of Transparent Nanostructured Electrodes for Modulation of Total Internal Reflection," in *Proc. of SPIE vol. 6647 Nanocoatings*, vol. 6647, p. 66470A, 2007.
- [66] C. Luo, S. Johnson, J. Joannopoulos, and J. Pendry, "All-angle negative refraction without negative effective index," *Physical Review B*, vol. 65, p. 201104, May 2002.
- [67] J. Chai, M. T. Taschuk, M. J. Brett, and J. M. Buriak, "Large area assembled periodic nanoarrays by block copolymer templating and glancing angle deposition," in *Nanostructured Thin Films* (G. B. Smith and

## REFERENCES

---

- A. Lakhtakia, eds.), vol. 7041, (San Diego, CA, USA), pp. 704111–10, SPIE, Aug. 2008.
- [68] T. Balla, S. M. Spearing, and A. Monk, “An assessment of the process capabilities of nanoimprint lithography,” *Journal of Physics D: Applied Physics*, vol. 41, p. 174001, Sept. 2008.
- [69] L. Guo, “Nanoimprint Lithography: Methods and Material Requirements,” *Advanced Materials*, vol. 19, pp. 495–513, Feb. 2007.
- [70] M. Bender, A. Fuchs, U. Platchetka, and H. Kurz, “Status and prospects of UV-Nanoimprint technology,” *Microelectronic Engineering*, vol. 83, pp. 827–830, Apr. 2006.
- [71] B. D. Gates, Q. Xu, M. Stewart, D. Ryan, C. G. Willson, and G. M. Whitesides, “New approaches to nanofabrication: molding, printing, and other techniques.,” *Chemical reviews*, vol. 105, pp. 1171–96, Apr. 2005.
- [72] S. Y. Chou, “Sub-10 nm imprint lithography and applications,” *Journal of Vacuum Science & Technology B: Microelectronics and Nanometer Structures*, vol. 15, p. 2897, Nov. 1997.
- [73] J. D. Krabbe and M. J. Brett, “Photonic crystal switching by the electrophoretic movement of dye ions,” in *Photonic and Phononic Crystal Materials and Devices X* (A. Adibi, S.-Y. Lin, and A. Scherer, eds.), vol. 7609, SPIE, 2010.
- [74] M. M. Hawkeye, *Engineering Optical Nanomaterials using Glancing Angle Deposition*. Phd, University of Alberta, 2010.
- [75] A. Fujishima, T. N. Rao, and D. A. Tryk, “Titanium dioxide photocatalysis,” *Journal of Photochemistry and Photobiology C: Photochemistry Reviews*, vol. 1, no. 1, pp. 1–21, 2000.
- [76] U. Diebold, “The surface science of titanium dioxide,” *Surface Science Reports*, vol. 48, no. 5-8, pp. 53–229, 2003.
- [77] J. D. Krabbe and M. J. Brett, “Photonic crystal reflectance switching by dye electrophoresis,” *Applied Physics Letters*, vol. 97, no. 4, p. 041117, 2010.
- [78] J. R. Taylor, *An Introduction to Error Analysis: The Study of Uncertainties in Physical Measurements*. University Science Books, 1996.
- [79] M. J. Colgan, B. Djurfors, D. G. Ivey, and M. J. Brett, “Effects of annealing on titanium dioxide structured films,” *Thin Solid Films*, vol. 466, no. 1-2, pp. 92–96, 2004.

## REFERENCES

---

- [80] L. Xiong, Y. Yang, J. Mai, W. Sun, C. Zhang, D. Wei, Q. Chen, and J. Ni, "Adsorption behavior of methylene blue onto titanate nanotubes," *Chem. Eng. J.*, vol. 156, no. 2, pp. 313–320, 2010.
- [81] M. Sahimi and V. L. Jue, "Diffusion of Large Molecules in Porous Media," *Phys. Rev. Lett.*, vol. 62, pp. 629–632, Feb. 1989.
- [82] W. M. Deen, "Hindered transport of large molecules in liquid-filled pores," *AIChE J.*, vol. 33, no. 9, pp. 1409–1425, 1987.
- [83] J. P. Dowling, M. Scalora, M. J. Bloemer, and C. M. Bowden, "The photonic band edge laser: A new approach to gain enhancement," *J. of Appl. Phys.*, vol. 75, no. 4, pp. 1896–1899, 1994.
- [84] F. A. Jenkins and H. E. White, *Fundamentals of Optics*. McGraw-Hill College, 1976.
- [85] D. F. Swinehart, "The Beer-Lambert Law," *Journal of Chemical Education*, vol. 39, p. 333, July 1962.
- [86] M. O. Jensen and M. J. Brett, "Square spiral 3D photonic bandgap crystals at telecommunications frequencies," *Optics Express*, vol. 13, no. 9, p. 3348, 2005.
- [87] E. Palik, *Handbook of optical constants of solids II*. Boston: Academic Press, 1991.
- [88] D. Vick, K. Krause, and M. Brett, "Focused Ion Beam Tomography of Porous Titania Thin Films," *Microscopy and Microanalysis*, vol. 15, p. 372, July 2009.
- [89] M. Malac, R. F. Egerton, M. J. Brett, and B. Dick, "Fabrication of submicrometer regular arrays of pillars and helices," *Journal of Vacuum Science & Technology B: Microelectronics and Nanometer Structures*, vol. 17, no. 6, p. 2671, 1999.
- [90] M. Jensen and M. Brett, "Periodically Structured Glancing Angle Deposition Thin Films," *IEEE Transactions On Nanotechnology*, vol. 4, pp. 269–277, Mar. 2005.
- [91] S. V. Kesapragada and D. Gall, "Two-component nanopillar arrays grown by Glancing Angle Deposition," *Thin Solid Films*, vol. 494, pp. 234–239, Jan. 2006.
- [92] J. Zhang, Y. Li, X. Zhang, and B. Yang, "Colloidal Self-Assembly Meets Nanofabrication: From Two-Dimensional Colloidal Crystals to Nanostructure Arrays," *Advanced materials (Deerfield Beach, Fla.)*, vol. 22, pp. 4249–69, Aug. 2010.

- [93] P. Jiang and M. J. McFarland, "Large-scale fabrication of wafer-size colloidal crystals, macroporous polymers and nanocomposites by spin-coating," *Journal of the American Chemical Society*, vol. 126, pp. 13778–86, Oct. 2004.
- [94] M. T. Taschuk, J. Chai, J. M. Buriak, and M. J. Brett, "Optical characterization of pseudo-ordered nanostructured thin films," *physica status solidi (c)*, pp. S127–S130, Apr. 2009.
- [95] I. Haller, M. Hatzakis, and R. Srinivasan, "High-resolution Positive Resists for Electron-beam Exposure," *IBM Journal of Research and Development*, vol. 12, pp. 251–256, May 1968.
- [96] A. N. Broers, "Resolution Limits of PMMA Resist for Exposure with 50 kV Electrons," *Journal of The Electrochemical Society*, vol. 128, no. 1, pp. 166–170, 1981.
- [97] M. Aktary, M. Stepanova, and S. K. Dew, "Simulation of the spatial distribution and molecular weight of polymethylmethacrylate fragments in electron beam lithography exposures," *Journal of Vacuum Science & Technology B: Microelectronics and Nanometer Structures*, vol. 24, no. 2, p. 768, 2006.